

## Unified Framework for Charge-Spin Interconversion in Spin-Orbit Materials

Shehrin Sayed<sup>1,2,\*</sup>, Seokmin Hong<sup>3,†</sup>, Xiaoxi Huang<sup>4</sup>, Lucas Caretta<sup>4,2</sup>, Arnoud S. Everhardt<sup>4</sup>,  
Ramamoorthy Ramesh<sup>4,2</sup>, Sayeef Salahuddin<sup>1,2</sup> and Supriyo Datta<sup>5,‡</sup>


<sup>1</sup>Electrical Engineering and Computer Sciences, University of California, Berkeley, California 94720, USA

<sup>2</sup>Materials Sciences Division, Lawrence Berkeley National Laboratory, Berkeley, California 94720, USA

<sup>3</sup>Center for Spintronics, Korea Institute of Science and Technology, Seoul 02792, Republic of Korea

<sup>4</sup>Materials Science and Engineering, University of California, Berkeley, California 94720, USA

<sup>5</sup>Electrical and Computer Engineering, Purdue University, West Lafayette, Indiana 47907, USA

 (Received 29 September 2020; revised 16 February 2021; accepted 2 April 2021; published 4 May 2021)

Materials with spin-orbit coupling are of great interest for various spintronics applications due to the efficient electrical generation and detection of spin-polarized electrons. Over the past decade, many materials have been studied, including topological insulators, transition metals, Kondo insulators, semimetals, semiconductors, and oxides; however, there is no unifying physical framework for understanding the physics and therefore designing a material system and devices with the desired properties. We present a model that binds together the experimental data observed on the wide variety of materials in a unified manner. We show that in a material with a given spin-momentum locking, the density of states plays a crucial role in determining the charge-spin interconversion efficiency, and a simple inverse relationship can be obtained. Remarkably, experimental data obtained over the last decade on many different materials closely follow such an inverse relationship. We further deduce two figure of merits of great current interest: the spin-orbit-torque (SOT) efficiency (for the direct effect) and the inverse Rashba-Edelstein effect length (for the inverse effect), which statistically show good agreement with the existing experimental data on wide varieties of materials. Particularly, we identify a scaling law for the SOT efficiency with respect to the carrier concentration in the sample, which agrees with existing data. Such an agreement is intriguing since our transport model includes only Fermi surface contributions and fundamentally different from the conventional views of the SOT efficiency that includes contributions from all the occupied states.

DOI: [10.1103/PhysRevApplied.15.054004](https://doi.org/10.1103/PhysRevApplied.15.054004)

### I. INTRODUCTION

Recently, charge-spin interconversion in various materials exhibiting spin-momentum locking (SML), e.g., topological insulators (TIs) [1–7], semiconductors [8,9], transition metals [10–18], semimetals [19], oxides [20–23], antiferromagnets [24], and superconductors [25], are growing interest for efficient spintronic applications. The sheer variety of materials is exciting, but it also poses a daunting challenge in understanding the underlying physics and designing devices for various applications with desired properties.

In this paper, we present a model (see Fig. 1) that binds together the charge-spin interconversion observed on the wide variety of materials in a unified manner using only four model parameters: the number of modes or density of states, the strength of SML, mean free path, and interface spin conductance. These four parameters are independently measurable and theoretically well understood. We show that, in a material with a given SML, the number of modes in the channel, which is related to the material density of states around the Fermi energy, plays a crucial role in determining the charge-spin interconversion efficiency. We point out a simple inverse relationship between the interconversion efficiency and the material density of states. Remarkably, experimental data obtained over the last decade on many different material systems closely follow this inverse relationship (see Fig. 2). We provide an intuitive understanding of the origin of such a scaling trend.

We discuss several figure of merits of great interest in emerging applications. We show that the charge-current-induced spin voltage and its reciprocal effect, which are

\*ssayed@berkeley.edu

†shong@kist.re.kr

‡datta@purdue.edu

Published by the American Physical Society under the terms of the [Creative Commons Attribution 4.0 International](https://creativecommons.org/licenses/by/4.0/) license. Further distribution of this work must maintain attribution to the author(s) and the published article's title, journal citation, and DOI.

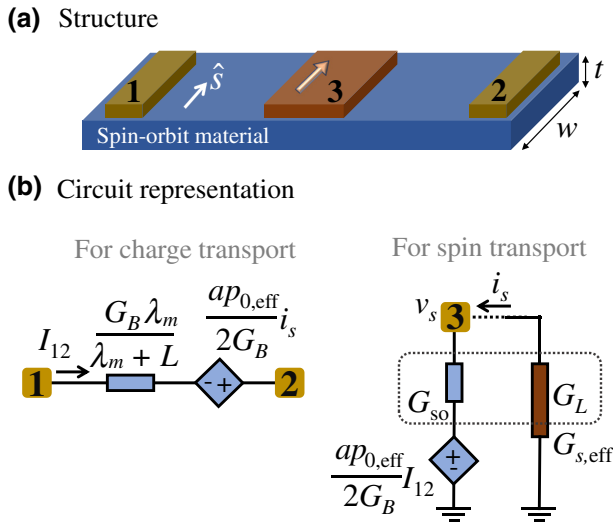


FIG. 1. (a) Three-terminal-based structure with a spin-orbit material. (b) Circuit representation for charge-to-spin conversion in a spin-orbit material.

of great interest to read out magnetization states in logic [26] and memory [27] applications, can be enhanced by lowering the density of states in a given material. We quantify the SML strength in various materials based on the available experimental data and compare it with the theoretical expectations from various origins of the SML. We further relate the four model parameters to widely used figure of merits: the spin-orbit-torque (SOT) efficiency (see Figs. 3 and 4) and the inverse Rashba-Edelstein effect (IREE) (see Fig. 5), which show good agreement with existing experiments. We show that the figure of merit for the spin voltage multiplied by the measured interface spin

conductance yields the SOT efficiency and also scales inversely with the number of modes in the channel. We identify a scaling law with the carrier concentration ( $n$ ) in the sample that the SOT efficiency  $\propto n^{-(2/3)}$ . Such a trend can be useful for future device design because the carrier concentration in various materials can be controlled with doping, electric gating, and strain modulation.

We derive the model from a semiclassical equation [28] that we previously obtained from the Boltzmann transport equation using four electrochemical potentials based on the sign of the group velocity and the spin index. Within our model, the transport parameters are described with electronic states around the Fermi energy, which is different from conventional views. Conventional models using the spin Berry curvature include contributions from all occupied states. By contrast, our model includes only Fermi surface contributions making it fundamentally different and this could help identify interesting results as the field evolves. For example, we discuss an interesting observation in recent experiments on correlated oxides [22,23] where the SOT efficiency decreased with the sample resistivity, contrary to the conventional view that the SOT efficiency increases in a resistive sample. We show that the experimental results closely follow the scaling trend of our model with respect to the measured carrier concentration. We briefly discuss the parameter conditions required to observe SOT efficiencies  $> 1$  within our model, which is of great current interest. In the present paper, we restrict our discussion to the cases where the SOT efficiencies are  $< 1$ .

The paper is organized as follows. In Sec. II, we present a resistance matrix model and describe its four key parameters. In Sec. III, we discuss charge-current-induced spin voltage and show that the spin voltage scales

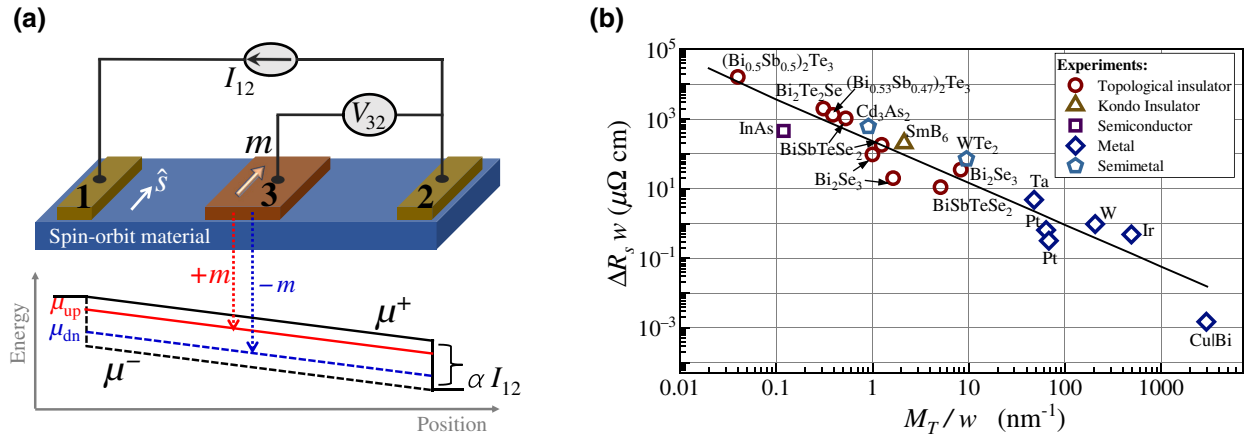


FIG. 2. (a) Setup to measure charge-current-induced spin voltage in a spin-orbit material using a ferromagnetic contact with magnetization  $m$ . (b) Charge-spin interconversion resistance,  $\Delta R_s$ , in diverse classes of materials as a function of channel number of modes ( $M_T$ ), which is related to the material density of states near the Fermi energy. Experimental data points include topological insulators [(Bi<sub>0.5</sub>Sb<sub>0.5</sub>)<sub>2</sub>Te<sub>3</sub> [4], (Bi<sub>0.53</sub>Sb<sub>0.47</sub>)<sub>2</sub>Te<sub>3</sub> [2], Bi<sub>2</sub>Se<sub>3</sub> [3,4,30], Bi<sub>2</sub>Te<sub>2</sub>Se [5], and BiSbTeSe<sub>2</sub> [7]], transition metals (Ta [31], Pt [31,32], W [31], and Ir [31]), metallic interface (Cu|Bi [33]), narrow bandgap semiconductor (InAs [8,9]), topological Kondo insulator (SmB<sub>6</sub> [34]), and semimetals (WTe<sub>2</sub> [19] and Cd<sub>3</sub>As<sub>2</sub> [44]). Solid black line represents the theoretical trend.

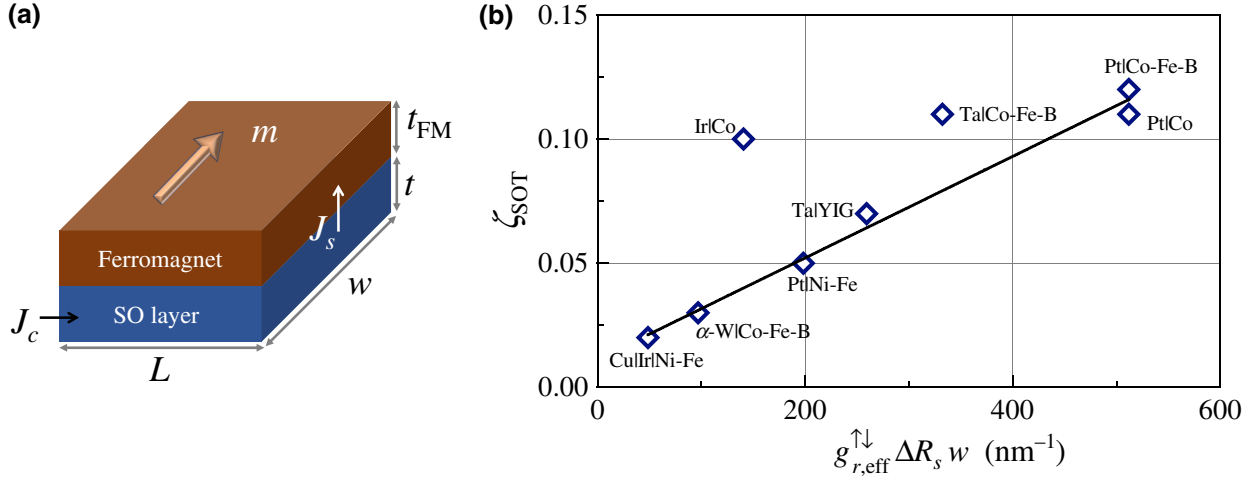


FIG. 3. (a) Structure for SOT-related experiments. (b) SOT efficiency  $\zeta_{SOT}$  in various metallic interfaces and comparison with Eq. (18).

inversely with the channel number of modes or material density of states over a broad range of materials. We extract the degree of spin-momentum locking in diverse materials and extend the spin-voltage model to derive a SOT efficiency model, which is in good agreement with the experiments on various materials. We also compare our model with conventional views. In Sec. IV, we discuss spin-current-induced charge voltage and extend the model to derive the inverse Rashba-Edelstein effect length, which shows good agreement with existing experiments on diverse materials. We end with a summary in Sec. V.

## II. RESISTANCE MATRIX MODEL

Our discussions in this paper are based on the following model for an arbitrary channel with SML:

$$\begin{Bmatrix} V_1 - V_2 \\ v_s \end{Bmatrix} = \begin{bmatrix} \frac{\lambda_m + L}{G_B \lambda_m} & -\frac{\alpha p_{0,eff}}{2G_B} \\ \frac{\alpha p_{0,eff}}{2G_B} & \frac{1}{G_{so}} \end{bmatrix} \begin{Bmatrix} I_{12} \\ i_s \end{Bmatrix}, \quad (1)$$

obtained from a semiclassical equation [28] in steady state, for a uniform structure with uniform spin potential and elastic scatterings in the channel, see Appendix A. Here  $V_{1,2}$  are the charge voltages on terminals 1 and 2,  $I_{12}$  is the charge current flowing in the channel,  $v_s$  is the spin voltage in the SML channel,  $i_s$  is the spin current injected from the SML channel to the adjacent layer,  $L$  is the channel length, and  $\alpha = 2/\pi$  is an angular averaging factor for the spin distribution in the channel. We represent Eq. (1) into a circuit in Fig. 1. Such a representation will be useful for a straightforward analysis of emerging devices and circuits implemented using spin-orbit materials.

A resistance matrix similar to Eq. (1) was reported in Ref. [28] for structures with nonmagnetic potentiometric (noninvasive) contacts on SML channels, which was derived under specific assumptions on the scattering mechanisms in the channel. Equation (1) in this paper applies to a structure with general scattering processes and arbitrary magnetic or nonmagnetic contacts. Although the resistance matrix in Eq. (1) is similar to Ref. [28], the effective model parameters are different and considers various possible origins of the SML.

The first diagonal term in Eq. (1) represents the charge resistance of the channel and the second diagonal term represents the spin source resistance that limits the spin-current injection into the adjacent layer. The off-diagonal terms indicate the coefficients for charge-spin interconversion. The model in Eq. (1) describes spin-dependent transport phenomena in terms of only four model parameters representing the channel:

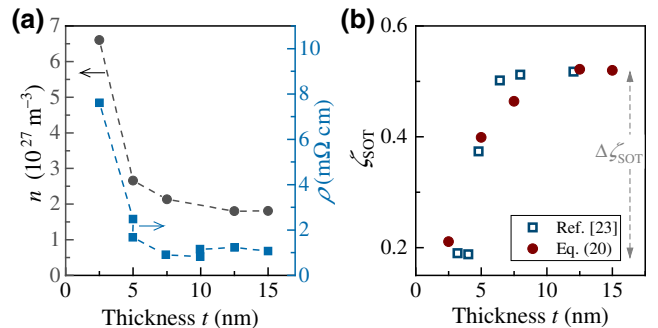


FIG. 4. (a) Resistivity and Hall carrier concentration of bare SrIrO<sub>3</sub> as a function of thickness, taken from Ref. [22]. (b) Spin-orbit torque (SOT) efficiency  $\zeta_{SOT}$  in SrIrO<sub>3</sub> calculated using Eq. (19) with carrier concentration in Fig. 4(a), and comparison with experiments in Ref. [23].

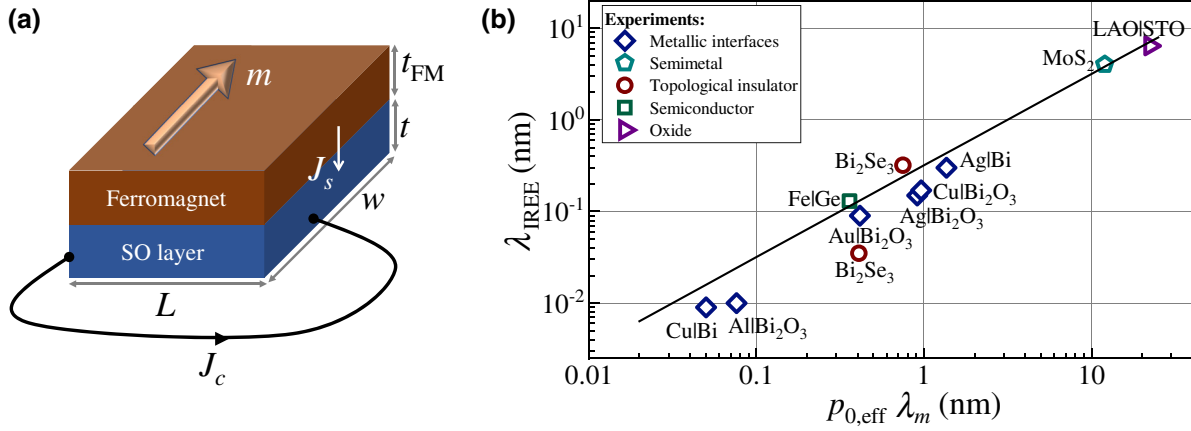


FIG. 5. (a) Structure for experiments on inverse effects. (b) Inverse Rashba-Edelstein effect length in diverse classes of materials including Ag|Bi [78], Cu|Bi [33], Ag|Bi<sub>2</sub>O<sub>3</sub> [84], Cu|Bi<sub>2</sub>O<sub>3</sub> [84], Au|Bi<sub>2</sub>O<sub>3</sub> [84], Al|Bi<sub>2</sub>O<sub>3</sub> [84], LaAlO<sub>3</sub>|SrTiO<sub>3</sub> (LAO|STO) [20], Bi<sub>2</sub>Se<sub>3</sub> [87], Fe/Ge(111) [85], and MoS<sub>2</sub> [86,97]. The solid line represents Eq. (32).

1.  $G_B = (q^2/h)M_T$  is a conductance parameter proportional to the total number of modes,  $M_T$ , in the channel ( $q$  is the electron charge and  $h$  is Planck's constant);
2.  $p_{0,\text{eff}}$  is the effective strength of the SML;
3.  $\lambda_m$  is the effective mean free path; and
4.  $G_{\text{so}}$  is the source conductance of the spin transport in the channel that limits the spin current extracted from the channel by a highly spin conductive load.

The details of the electronic structure of the materials, growth conditions, and different physical structures and interfaces could result in different effective values of the parameters; however, the general scaling law presented in the paper holds and statistically shows a good agreement with a large number of experimental data. The parameters are described in detail below.

#### A. Channel number of modes and the material density of states

The conductance parameter  $G_B$  in Eq. (1) represents the total number of modes,  $M_T$ , in the channel, given by

$$G_B = \frac{q^2}{h} M_T. \quad (2)$$

The total number of modes in the channel is related to the density of states around the Fermi energy per unit length of the channel,  $D$ , and the group velocity of the electronic states,  $v$ , as given by [29]

$$M_T = \frac{hDv}{2} \eta, \quad (3)$$

where  $\eta$  is a geometrical factor, which is 1,  $2/\pi$ , and  $1/2$  in a one-dimensional (1D), two-dimensional (2D), and three-dimensional (3D) channel, respectively.  $M_T$  represents the number of electron wavelengths that fit into the channel

cross section [29] and related to the carrier concentration in the sample as

$$\frac{M_T}{wt} = \sqrt[3]{\frac{9\pi}{8}} n_s^{\frac{2}{3}}, \quad (\text{for a 3D channel}), \quad (4a)$$

$$\frac{M_T}{w} = \sqrt{\frac{2}{\pi}} n_s^{\frac{1}{2}}, \quad (\text{for a 2D channel}), \quad (4b)$$

where  $n_s$  and  $n$  are the carrier concentrations in a 2D and a 3D channel, respectively,  $w$  is the width, and  $t$  is the thickness of the channel. See Appendix B.

#### B. Strength of the spin-momentum locking

The parameter  $p_{0,\text{eff}}$  in our model quantifies the strength of SML in an arbitrary channel.  $p_{0,\text{eff}}$  has two components:

$$p_{0,\text{eff}} = \epsilon p_0 + p_{rs},$$

where  $\epsilon$  a unitless parameter that depends on the contact conductance, contact polarization, and scattering rates in the channel. The component proportional to  $p_{rs}$  is induced by impurities that can cause a difference in the scattering rates between up and down polarized states, which is explained in detail in Appendix A.

The component proportional to  $p_0$  is induced from the band structure of the material, which is given by [28]

$$p_0 = \frac{M - N}{M + N}, \quad (5)$$

where  $M$  is the number of modes for the up (and down) spin-polarized electronic states with the positive (and the negative) group velocity, see Appendix A. Similarly,  $N$  is the number of modes for the down (and up) spin-polarized

electronic states with the positive (and the negative) group velocity. The total number of modes  $M_T = M + N$ . The parameter  $p_0$  varies between 0 and 1.  $p_0 = 0$  represents a normal metal, where up and down spin-polarized states have the same number of modes in the channel for positive and negative group velocities (i.e.,  $M = N$ ) and the channel exhibits no SML.  $p_0 = 1$  (i.e.,  $N = 0$ ) represents a perfect SML where all electronic states with positive group velocity are up spin polarized, and all electronic states with negative group velocity are down spin polarized. Such a perfect SML is observed for an ideal topological band insulator.

For a general SML channel, the value of  $p_0$  can be any value between 0 and 1 and depends on the underlying band structure and origin of the SML. For example, for a Rashba channel, Eq. (5) becomes (see Appendix C)

$$p_0 = \frac{\alpha_R}{\sqrt{\alpha_R^2 + (\hbar v_F)^2}}, \quad (6)$$

where  $\alpha_R$  is the Rashba coefficient,  $v_F$  is the Fermi velocity, and  $\hbar = h/(2\pi)$  is the reduced Planck constant. For weak Rashba channels,  $p_0 \approx \alpha_R/(\hbar v_F) \ll 1$ .

Note that  $p_{0,\text{eff}}$  can be nonzero even in a normal metal ( $p_0 = 0$ ) due to a contribution from  $p_{rs}$ , if we can introduce impurities that can induce a difference in the scattering rates between up and down spin-polarized states, as described in Appendix A. In this paper, we do not assume any particular origin of  $p_{0,\text{eff}}$ . We keep the parameter  $p_{0,\text{eff}}$  general and extract it from existing experiments and comment on its strength based on results on known systems. We show that for a given  $p_{0,\text{eff}}$  how the density of states or number of modes plays a crucial role in determining the efficiency of charge-spin interconversion.

### C. Mean free path

The mean free path,  $\lambda_m$ , refers to the backscattering length of electrons, which determines the charge resistance of the sample. The mean free path and the total number of modes ( $M_T$ ) in the channel are related to the measured resistivity ( $\rho$ ) and sheet resistance ( $R_{\text{sheet}}$ ) as

$$\frac{\rho}{wt} = \frac{R_{\text{sheet}}}{w} = \frac{h}{q^2 M_T \lambda_m}. \quad (7)$$

### D. Spin source conductance

Spin-orbit materials generate nonequilibrium spins, which can be injected into an adjacent layer. The internal spin source conductance,  $G_{\text{so}}$ , limits the spin current injected into a highly spin conductive layer, similar to the internal source resistance of a battery. In our model,  $G_{\text{so}}$  is

given by

$$G_{\text{so}} = \frac{4G_B L_f}{\alpha^2 (1 - p_0^2) \lambda_{s0}}, \quad (8)$$

see Appendix A for details. Here,  $\lambda_{s0}$  is a spin-dependent scattering length, and  $L_f$  is the length of the ferromagnet. Equation (8) [a component of Eq. (1)] is derived under the assumption of elastic scatterings, uniform structure, and uniform spin potential in the channel. The assumptions can be revisited as the field evolves, which may result in an effective change in the values of the model parameters; however, the general structure of Eq. (1) will not change.

In the presence of an adjacent layer with spin conductance  $G_L$ , see Fig. 1, the effective conductance,  $G_{s,\text{eff}}$ , that determines the injected spin current is given by

$$G_{s,\text{eff}} = \frac{G_{\text{so}} G_L}{G_{\text{so}} + G_L}. \quad (9)$$

For an adjacent ferromagnetic contact,  $G_L$  is modeled with the bare interface spin-mixing conductance [35,36]. When the magnetization  $\vec{m}$  is perpendicular to the spin polarization  $\hat{s}$ ,  $G_L$  is the real part of the spin-mixing conductance  $G_r^{\uparrow\downarrow}$  [35,36], and  $G_{s,\text{eff}}$  is typically expressed in terms of an effective spin-mixing conductance,  $g_{r,\text{eff}}^{\uparrow\downarrow}$ , in the units of  $m^{-2}$ , as given by

$$G_{s,\text{eff}} = \frac{G_{\text{so}} G_r^{\uparrow\downarrow}}{G_{\text{so}} + G_r^{\uparrow\downarrow}} = \frac{2q^2}{h} g_{r,\text{eff}}^{\uparrow\downarrow} w_f L_f, \quad (10)$$

where  $g_{r,\text{eff}}^{\uparrow\downarrow}$  can be measured from ferromagnetic resonance experiments on the bilayer [37–39]. Here,  $w_f$  and  $L_f$  are the width and length of the FM layer.

## III. DIRECT EFFECT: CHARGE-TO-SPIN CONVERSION

### A. Figure of merit for charge-current-to-spin-voltage conversion

#### 1. Model

A charge current  $I_{12}$  in a spin-orbit (SO) material induces a spin voltage  $v_s$  [28,40]. In the absence of any adjacent layer, i.e.,  $G_L \rightarrow 0$  in Fig. 1(b),  $v_s$  is given by

$$v_s = \frac{\alpha p_{0,\text{eff}}}{2G_B} I_{12}. \quad (11)$$

The spin voltage in the channel can be measured in the form of an open-circuit charge voltage using a FM contact with its magnetization ( $m$ ) along the spin-polarization axis ( $\hat{s}$ ) in the channel [40,41]. The charge voltage difference

between the two magnetic states ( $+m$  and  $-m$ ) is proportional to  $v_s$ , as given by [see Fig. 2(a)]

$$\Delta V = V_{32}(+m) - V_{32}(-m) = \frac{\alpha \xi p_{0,\text{eff}} p_f}{G_B} I_{12}, \quad (12)$$

where  $\xi = G_{\text{so}} / (G_{\text{so}} + G_L)$ . The method has been used on diverse classes of materials, including, topological insulators [1–7], transition metals [31,32,42], semiconductors [8], Kondo insulators [34], and semimetals [19], using both potentiometric and Ohmic FM contacts.

The figure of merit for a material's capability to convert a charge current into a spin voltage is  $\Delta R_S = \Delta V / I_{12}$ , which we define as the charge-spin interconversion resistance. We multiply both sides with  $w$  to make it in the unit of resistivity

$$\Delta R_S \times w = \frac{\Delta V}{I_{12}} \times w = \frac{h}{q^2} \frac{\alpha \xi p_{0,\text{eff}} p_f}{M_T / w}, \quad (13)$$

which also ensures that the experimental data points discussed in Fig. 2(b) are independent of the channel width.

Equation (12) describes a charge-current-induced spin voltage in a conductor with nonzero density of states ( $D$ ) around the Fermi energy. For a fixed charge current ( $I_{12}$ ), the spin voltage scales inversely with  $M_T$  or  $D$  around the Fermi energy and we expect a large spin voltage in a material with an arbitrarily small  $D$ . However, a lower  $D$  also yields a higher channel resistivity and a larger voltage drop across the channel length ( $V_1 - V_2$ ) is required to inject a sizable  $I_{12}$  in the channel. For negligible spin current

( $i_s \approx 0$ ), we can derive an expression for  $\Delta V / (V_1 - V_2)$  from Eq. (1) as

$$\left. \frac{\Delta V}{V_1 - V_2} \right|_{i_s=0} = 2p_f \frac{\lambda_{\text{IREE}}}{\lambda_m + L}, \quad (14)$$

where  $\lambda_{\text{IREE}}$  is given by Eq. (32) and is discussed later. Note that the ratio of the open-circuit spin voltage to the applied charge voltage across the channel length in Eq. (14) is independent of  $M_T$ .

## 2. Comparison with experiments

In Fig. 2(b), we compare Eq. (13) with experimentally measured  $\Delta R_S \times w$  on a wide variety of materials as a function of  $M_T / w$  of the corresponding device. We consider a diverse classes of materials with a large range of variations in the density of states, including, topological insulators [(Bi<sub>0.5</sub>Sb<sub>0.5</sub>)<sub>2</sub>Te<sub>3</sub> [4], (Bi<sub>0.53</sub>Sb<sub>0.47</sub>)<sub>2</sub>Te<sub>3</sub> [2], Bi<sub>2</sub>Se<sub>3</sub> [3,4,30], Bi<sub>2</sub>Te<sub>2</sub>Se [5], and BiSbTeSe<sub>2</sub> [7]], transition metals (Ta [31], Pt [31,32], W [31], and Ir [31]), metallic interfaces (Cu|Bi [33]), narrow band-gap semiconductors (InAs [8,9]), topological Kondo insulators (SmB<sub>6</sub> [34]), and semimetals (WTe<sub>2</sub> [19], Cd<sub>3</sub>As<sub>2</sub> [44]). We estimate  $M_T$  from the measured carrier concentration using Eq. (4) or from the measured resistivity or sheet resistance and known mean free path using Eq. (7). The details of the data points and related estimations are summarized in Tables I–II, with detailed footnotes.

Remarkably, the spin voltage in diverse classes of spin-orbit materials (both topological and nontopological) are scaling inversely proportional to the total number of modes

TABLE I. Charge-spin interconversion resistance in diverse materials.

SOC material	Ferromagnet ( $p_f$ )	$\Delta R_S$ ( $\Omega$ )	$w$ ( $\mu\text{m}$ )	$t$ (nm)	$\Delta R_S \times w$ ( $\mu\Omega \text{cm}$ )
(Bi <sub>0.5</sub> Sb <sub>0.5</sub> ) <sub>2</sub> Te <sub>3</sub> [4]	Co-Fe-B MgO (0.5)	20	8	7	16 000
(Bi <sub>0.53</sub> Sb <sub>0.47</sub> ) <sub>2</sub> Te <sub>3</sub> [2]	Co Al <sub>2</sub> O <sub>3</sub> (0.42)	5.2	2.5	9	1300
Bi <sub>2</sub> Se <sub>3</sub> [30]	Co TiO <sub>2</sub> (0.3)	0.2	1	20	20
Bi <sub>2</sub> Se <sub>3</sub> [3]	Co TiO <sub>2</sub> (0.2)	0.07	5	40	35 (dev 1)
Bi <sub>2</sub> Se <sub>3</sub> [4]	Co-Fe-B MgO (0.5)	0.12	8	7	96
Bi <sub>2</sub> Te <sub>2</sub> Se [5]	Ni-Fe Al <sub>2</sub> O <sub>3</sub> (0.45)	2.2	9	10	1980
BiSbTeSe <sub>2</sub> [7]	Ni-Fe MgO (0.45)	0.013	8.5	172	11 (dev 1)
		0.4	4.5	82	180 (dev 2)
		1.6	6.5	54	1040 (dev 3)
SmB <sub>6</sub> [34]	Ni-Fe AlO <sub>x</sub> (0.38)	0.004	500	–	200
Cu Bi [33]	Ni-Fe (0.31) [43]	$1 \times 10^{-4}$	0.15	100	$1.5 \times 10^{-3}$
Pt [32]	Co-Fe (0.58)	$8 \times 10^{-3}$	0.4	7	0.32
Pt [31]	Co-Fe-B MgO (0.6)	$0.8 \times 10^{-3}$	8	7	0.64
Ta [31]	Co-Fe-B MgO (0.6)	$6 \times 10^{-3}$	8	7	4.8
W [31]	Co-Fe-B MgO (0.6)	$1.2 \times 10^{-3}$	8	7	0.96
Ir [31]	Co-Fe-B MgO (0.6)	$0.6 \times 10^{-3}$	8	7	0.48
WTe <sub>2</sub> [19]	Ni-Fe (0.45)	0.14	5	23	70
Cd <sub>3</sub> As <sub>2</sub> [44]	Co oxide (0.4)	40	0.15 <sup>a</sup>	–	600
InAs [8]	Ni-Fe Al <sub>2</sub> O <sub>3</sub> (0.5)	0.56	8	2	448

<sup>a</sup>Diameter of the nanowire.

TABLE II. Estimation of the number of modes and degree of spin-momentum locking in diverse materials.

SOC material	$n$ ( $\times 10^{25} \text{ m}^{-3}$ )	$n_s$ ( $\times 10^{16} \text{ m}^{-2}$ )	$k_F^i$ ( $\text{nm}^{-1}$ )	$\rho$ ( $\mu\Omega \text{ cm}$ )	$R_{\text{sheet}}$ ( $\Omega$ )	$\lambda_m$ (nm)	$M_T/w$ ( $\text{nm}^{-1}$ )	$p'_{0,\text{eff}}$ [Eq. (13)]
(Bi <sub>0.5</sub> Sb <sub>0.5</sub> ) <sub>2</sub> Te <sub>3</sub>	—	—	—	—	6000 [4]	150 [4]	0.029 [Eq. (7)]	0.56
(Bi <sub>0.53</sub> Sb <sub>0.47</sub> ) <sub>2</sub> Te <sub>3</sub>	0.47 <sup>b</sup>	—	0.52	—	—	—	0.39 [Eq. (4)]	0.73
Bi <sub>2</sub> Se <sub>3</sub>	1.25 [30]	—	0.72	—	—	—	1.64 [Eq. (4)]	0.066
Bi <sub>2</sub> Se <sub>3</sub>	5 [3]	—	1.14	—	18 [3]	130 [4]	8.3 [Eq. (4)] 11 [Eq. (7)]	0.88
Bi <sub>2</sub> Se <sub>3</sub>	3 [4]	—	0.96	—	—	—	1 [Eq. (4)]	0.12
Bi <sub>2</sub> Te <sub>2</sub> Se	—	—	0.44 [45]	—	—	—	0.31 [Eq. (4)]	0.83
BiSbTeSe <sub>2</sub>	0.26 <sup>c</sup> (dev 1)	—	0.43	—	—	—	4.95 [Eq. (4)]	0.073
	0.1 <sup>c</sup> (dev 2)	—	0.31	—	—	—	1.25 [Eq. (4)]	0.3
	0.056 <sup>c</sup> (dev 3)	—	0.25	—	—	—	0.56 [Eq. (4)]	0.79
SmB <sub>6</sub>	—	—	6.7 [34]	—	—	—	2.13 [Eq. (4)]	0.68
Cu Bi	8470 <sup>d</sup> [46]	—	13.6	—	—	—	2938 [Eq. (4)]	0.0086 <sup>e</sup>
Pt	—	—	—	27 [31]	—	10.5 <sup>a</sup> [47]	63.9 [Eq. (7)]	0.021 (from Ref. [32])
	1600 [47]	—	7.8	—	—	—	67.7 [Eq. (4)]	0.044 (from Ref. [31])
Ta	—	—	—	210 [31]	—	1.8 <sup>f</sup>	47.9 [Eq. (7)]	0.23
W	—	—	—	42 [31]	—	2.1 <sup>f</sup>	205.4 [Eq. (7)]	0.2
Ir	—	—	—	28 [31]	—	1.32 <sup>g</sup>	490.2 [Eq. (7)]	0.24
WTe <sub>2</sub>	—	1.9 [19]	0.35	—	—	—	9.5 [Eq. (4)]	0.9
Cd <sub>3</sub> As <sub>2</sub>	0.036 [44]	—	0.22	—	—	—	1.02 <sup>h</sup> [Eq. (4)]	0.93
InAs	—	2 [8]	0.36	—	—	—	0.23 [Eq. (4)]	0.12

<sup>a</sup>The reported mean free path is for samples with similar resistivity (approximately 20  $\mu\Omega \text{ cm}$ ).

<sup>b</sup>Calculated using  $n = n_s/t$  with  $n_s = 4.25 \times 10^{16} \text{ m}^{-2}$  [2].

<sup>c</sup>We use  $B/(ntq)$  to extract  $n$  from their ordinary Hall resistance measurements on three different devices (dev 1, dev 2, and dev 3), where  $B$  is the external magnetic field.

<sup>d</sup>We assume that most of the current conduction occurs in the conductive layer Cu and calculated the total number of modes based on Cu parameters.

<sup>e</sup> $p_0$  estimated from Eq. (6) is approximately 0.296 using  $\alpha_R = 3.2 \times 10^{-10} \text{ eV m}$  [48] and  $v_F = 1.57 \times 10^6 \text{ ms}^{-1}$  for Cu [46]. Note:  $v_F = 1.87 \times 10^6 \text{ ms}^{-1}$  for Bi [46]. Estimation from the experiment in Ref. [33] is much lower than this theoretical value and could be due to a higher current shunting in the magnetic contact.

<sup>f</sup>We assume  $\lambda_m$  to be equal to the spin-diffusion lengths reported in Refs. [13] and [14], it was pointed out previously that they are comparable [49].

<sup>g</sup> $\lambda_m$  for Ir reported in Ref. [50] is 7.09 nm for a sample with  $\rho = 5.2 \mu\Omega \text{ cm}$ . We assume a 5.4 times smaller value since the resistivity of the sample in Ref. [31] is 5.4 times higher.

<sup>h</sup>The channel is a nanowire with a cross-section  $\pi r^2$  ( $r$  is the radius). We have approximated  $w = t = \sqrt{\pi r}$ .

<sup>i</sup>These values are estimated using  $k_F = \sqrt{3\pi^2 n}$  or  $k_F = \sqrt{2\pi n_s}$  [28], or taken from corresponding references.

in the material, as described by Eq. (12). Although the data points are scattered in nature due to a variation of  $t$ ,  $p_{0,\text{eff}}$ ,  $p_f$ , and  $\xi$  from sample to sample, we observe a 7 orders of magnitude enhancement in the charge-spin interconversion resistance ( $\Delta R_s$ ) due to a 7 orders of magnitude lowering in the number of modes ( $M_T$ ) over the diverse classes of materials shown in Fig. 2(b). This implies that the density of states or number of modes plays a dominant role in determining  $\Delta R_s$ . This observation is interesting and could be useful for spin-voltage-based logic and memory applications, because the density of states can be externally controlled with gate-induced electronic fields on semiconductors and using strain on various oxides.

Note that some data points on topological materials in Fig. 2(b) correspond to low-temperature experiments,

and the spin signals in these experiments decreases with the temperature. The temperature-dependent degradation is known to arise from the topological surface states formation conditions, positioning of the Fermi level in the topological bands, the coexistence of parallel channels, contact polarization degradation, etc., which are related to  $\xi p_{0,\text{eff}} p_f$  in Eq. (12). In Fig. 2(b), we take the maximum reported values of  $\Delta R_s$  in various materials and plot them against their corresponding number of modes to illustrate how the density of states play a crucial role in the scaling of the spin voltage.

### 3. Anatomy of Eq. (11)

Equation (11) can be decomposed into (i) the standard mesoscopic view for charge current and (ii) the

conventional definition of spin-momentum locking. The mesoscopic view [51] assigns two electrochemical potentials,  $\mu^+$ , and  $\mu^-$ , to electronic states with positive and negative group velocities, respectively. The charge current in the channel is related to  $\mu^+$  and  $\mu^-$  as

$$I_{12} = \frac{G_B}{q} (\mu^+ - \mu^-) = \frac{q}{h} M_T (\mu^+ - \mu^-), \quad (15)$$

which indicates that  $\mu^+ - \mu^-$  is proportional to  $I_{12}$  and inversely proportional to  $M_T$ . Note that Eq. (15) is valid for transport in the linear regime in any materials, with or without the SML.

A perfect SML means electronic states with the positive group velocity are all up spin polarized; hence,  $\mu^+$  represents an up spin potential,  $\mu_{\text{up}}$ . On the other hand, electronic states with the negative group velocity are all down spin polarized; hence,  $\mu^-$  represents a down spin potential,  $\mu_{\text{dn}}$ . In such an ideal scenario, we have

$$\mu^+ - \mu^- = \mu_{\text{up}} - \mu_{\text{dn}},$$

where spin voltage is  $v_s = (\mu_{\text{up}} - \mu_{\text{dn}})/2$ . However, in real materials, the spin voltage is reduced by a lower strength of SML ( $p_0$ ), spin-dependent scatterings in the channel ( $\epsilon$ ), and angular distribution of the spin-polarized states around the spin quantization axis ( $\alpha$ ), as given by

$$\mu_{\text{up}} - \mu_{\text{dn}} = \alpha p_{0,\text{eff}} (\mu^+ - \mu^-). \quad (16)$$

Combining Eqs. (15) and (16) yields Eq. (11). Note that the observation in Fig. 2(b) that the spin signals scales inversely with  $M_T$ , originates from the mesoscopic view of charge current transport in Eq. (15). This feature is reflected on  $v_s$  when spin polarization becomes locked to the momentum.

## B. Strength of the spin-momentum locking in various materials

### 1. SML strength in topological materials

We extract the effective strength of SML  $p'_{0,\text{eff}} = \xi p_{0,\text{eff}}$  from the experimental data points in Fig. 2 using Eq. (13) and summarize them in Table II. An ideal topological insulator is expected to show  $p_{0,\text{eff}} = 1$ . The estimated values of  $p'_{0,\text{eff}}$  from experiments are close to 1 for the materials known to exhibit topological surface states, e.g.,  $(\text{Bi}_{0.5}\text{Sb}_{0.5})_2\text{Te}_3$ ,  $\text{BiSbTeSe}_2$ ,  $\text{Bi}_2\text{Te}_2\text{Se}$ , and  $\text{Bi}_2\text{Se}_3$ . Although,  $p'_{0,\text{eff}}$  estimated from the spin voltage measured on the  $\text{Bi}_2\text{Se}_3$  sample in Ref. [30] is much lower and could originate from a Rashba channel that can coexist in such material [52,53]. Note that the  $p'_{0,\text{eff}}$  estimated on other topological materials are also close to unity, e.g., topological Kondo insulator  $\text{SmB}_6$  [34], topological Weyl semimetal  $\text{WTe}_2$  [19], and a topological Dirac semimetal  $\text{Cd}_3\text{As}_2$ , indicating a strong SML as expected.

### 2. SML strength in Rashba channels

For the Cu|Bi interface, the estimated  $p'_{0,\text{eff}}$  is approximately 0.0086, which is very weak. The Cu|Bi interface is a weak Rashba channel with a theoretical strength of the SML  $p_0 \approx \alpha_R/(\hbar v_F) \approx 0.054$  calculated using  $\alpha_R = 5.6 \times 10^{-11}$  eV m [33] and  $v_F = 1.57 \times 10^6$  ms<sup>-1</sup> (for Cu) [46] in Eq. (6). This lowering from the theoretical value can be attributed to a lower  $\xi$  (approximately 0.16) since the ferromagnet in Ref. [33] is in direct contact with the metallic channel. Two-dimensional electron gas in an InAs quantum well is known as a strong Rashba channel, and  $p'_{0,\text{eff}}$  estimated from the experiment is large approximately 0.12.

### 3. SML strength in metals

The  $p'_{0,\text{eff}}$  extracted for Pt is in the order of that observed in a weak Rashba channel. Measurements on Pt in Ref. [31] were done with an oxide barrier at the interface and the extracted  $p'_{0,\text{eff}} \approx 0.044$ . However, the estimated  $p'_{0,\text{eff}} \approx 0.021$  is lower for Pt in Ref. [32], where the ferromagnet was in direct contact with the channel. Such lowering could be attributed to a lower  $\xi$  due to such direct contact. The extracted values of  $p'_{0,\text{eff}}$  for Ta, W, and Ir are large (approximately 0.2), in the order typically observed in a strong Rashba channel or a topological material with parallel channels. The origin of the SML in transition metals is a topic of active debate and could involve a bulk mechanism [13,36] or an interface Rashba-like mechanism [54–58]. Irrespective of the underlying mechanism, as long as there is a measurable spin voltage at the ferromagnetic contact, we can extract the strength of SML using Eq. (12).

## C. Figure of merit for the charge-current-to-spin-current conversion

### 1. Model for spin-orbit-torque efficiency

The spin voltage,  $v_s$ , in the SO layer will inject a spin current,  $i_s$ , in the adjacent FM layer, given by

$$i_s = G_{s,\text{eff}} \times v_s, \quad (17)$$

derived from the circuit in Fig. 1(b). Here,  $G_{s,\text{eff}}$  is given by Eq. (9)–(10) and  $v_s$  is given by Eqs. (11)–(12). The spin current,  $i_s$ , applies a torque to the adjacent FM and the torque is maximum when  $\vec{m} \perp \hat{s}$ . A widely used figure of merit for charge-current-to-spin-current conversion is the SOT efficiency  $\zeta_{\text{SOT}} = J_s/J_c$ . We derive a model for  $\zeta_{\text{SOT}}$  by combining Eq. (17) with Eqs. (10) and (11), as given by

$$|\zeta_{\text{SOT}}| = \frac{|J_s|}{|J_c|} = \frac{q^2}{h} g_{r,\text{eff}}^{\uparrow\downarrow} \times \frac{\Delta R_s w t}{p_f}, \quad (18)$$

where  $J_s = i_s/(w_f L_f)$  and  $J_c = I_{12}/(w t)$ . Interestingly, Eq. (18) indicates  $\zeta_{\text{SOT}}$  is determined by both the SO layer



and the magnetic interface and two independent measurements,  $\Delta R_s$  from spin potentiometric experiments in Fig. 2 and  $g_{r,\text{eff}}^{\uparrow\downarrow}$  from FM resonance experiments, can be multiplied together to estimate the SOT efficiency in a device. Equation (18) also indicates that it is possible that  $\zeta_{\text{SOT}}$  is substantially different in a SO material when coupled to a different FM interface.

We combine Eq. (18) with Eq. (13) to get the following analytical expression, given by

$$|\zeta_{\text{SOT}}| = \alpha p'_{0,\text{eff}} \times \frac{g_{r,\text{eff}}^{\uparrow\downarrow}}{m_n}, \quad (19)$$

where  $m_n = M_T/(wt)$  is the total number of modes per unit cross-section area of the channel. Note that  $\zeta_{\text{SOT}}$  also scales inversely with the channel number of modes or the density of states around the Fermi energy in the material. This inverse scaling with  $m_n$  can be related to the generally observed trend that resistive materials lead to higher SOT efficiency (see, e.g., Refs. [59,60]), because the conductivity ( $\sigma$ ) of the material is related to the  $m_n$  as  $\sigma = 1/\rho = (q^2/h)m_n\lambda_m$  [see Eq. (7)].

We combine Eq. (19) with the expression for  $m_n$  in Eq. (4a) and get the following expression:

$$|\zeta_{\text{SOT}}| = \left(\frac{8}{3\pi^2}\right)^{\frac{2}{3}} \frac{p'_{0,\text{eff}} g_{r,\text{eff}}^{\uparrow\downarrow}}{n^{\frac{2}{3}}}, \quad (20)$$

which indicates a scaling trend of  $\zeta_{\text{SOT}} \propto n^{-(2/3)}$  with respect to the carrier concentration in the sample. Such a trend could be useful for future device design, as carrier concentration can be controlled with doping, electric gating, and strain modulation. Note that our model

for the SOT efficiency describes the transport with electronic states only around the Fermi level, which is quite different from conventional views [60,61] that consider all the occupied states. We discuss this difference in the Sec. III D.

## 2. SOT efficiencies in metals

We use  $\Delta R_s$  data from Table I for SO materials and calculate the effective SOT efficiency using reported  $g_{r,\text{eff}}^{\uparrow\downarrow}$  on various SO|FM interfaces. The calculations are summarized in Table III. The calculated values of  $\zeta_{\text{SOT}}$  using Eq. (18) are compared with existing experiments on various metals in Table III and in Fig. 3, which show good agreement. Note that the calculated  $\zeta_{\text{SOT}}$  for W is close to the experimental report for  $\alpha$ -W because the spin voltage value used was measured in Ref. [31] on a sample with resistivity similar to that typically observed in  $\alpha$ -W [62].  $\zeta_{\text{SOT}}$  is higher on resistive W samples, e.g.,  $\beta$ -W [14] or amorphous  $a$ -W [62]. In Fig. 3, we compare Eq. (18) with experiments on well-known metallic systems: Pt|Ni-Fe, Pt|Fe-Co-B, Pt|Co, Ta|Co-Fe-B, Ta|YIG, W|Co-Fe-B, and Ir|Co, which show reasonably good agreement. Note that Eq. (18) is applicable to other emerging materials as well, which we have discussed in Tables III and IV.

We estimate  $p'_{0,\text{eff}}$  for various known metallic Rashba interfaces from the reported Rashba coefficient  $\alpha_R$  and Fermi velocity  $v_F$  using Eq. (6). Interestingly, the calculated  $\zeta_{\text{SOT}}$  using such theoretical estimations of  $p'_{0,\text{eff}}$  matches reasonably well with measured  $\zeta_{\text{SOT}}$  on Au|FM, and Ag|Bi|Ni-Fe. Here,  $m_n$  is estimated from the carrier density of the corresponding conductive layers using Eq. (4), and  $g_{r,\text{eff}}^{\uparrow\downarrow}$  is taken from measured values in the literature. The results are summarized in Table IV.  $\zeta_{\text{SOT}}$

TABLE III. SOT efficiencies in various materials estimated from charge-spin interconversion resistance and interface spin conductance.

SOC material	$\frac{\Delta R_s \times w \times t}{P_f}$ ( $\Omega \text{ nm}^2$ )	$g_{r,\text{eff}}^{\uparrow\downarrow}$ ( $\text{nm}^{-2}$ )	$ \zeta_{\text{SOT}} $ [from Eq. (18)]	$ \zeta_{\text{SOT}} $ (measured)
Pt   Ni-Fe	74.7	15.2 [11]	0.044	0.05 [11]
Pt   Fe-Co-B		40 [98]	0.115	0.12 [12]
Pt   Co		39.6 [11]	0.114	0.11 [11]
Ta   Co-Fe-B	560	6.92 [67]	0.15	0.12 $\pm$ 0.04 [13]
Ta   YIG		5.4 [68]	0.11	0.07 [68]
W   Co-Fe-B	112	10.1 [69]	0.044	0.33 ( $\beta$ -W [14]) 0.03 ( $\alpha$ -W [62]) 0.2 $\sim$ 0.5 ( $a$ -W [62])
Ir   Co	56	29.3 [70]	0.063	0.1 [15]
Cu   Ir   Ni-Fe	56	10.1 [77]	0.022	0.02 [16]
Bi <sub>2</sub> Se <sub>3</sub>  Ni-Fe	13 333.33	12 $\sim$ 65 [71]	6.2 $\sim$ 33.5	2 $\sim$ 3.5 [37]
	70 000		32.5 $\sim$ 175.8	1.56 $\sim$ 18.62 [72]
	13 440		6.2 $\sim$ 33.8	
WTe <sub>2</sub>	35 777.8	15.8	21.84	0.23 $\sim$ 0.79 [73]

TABLE IV. SOT efficiencies in Rashba channels.

Material	$n$ ( $\times 10^{28} \text{ m}^{-3}$ )	$k_F$ ( $\text{nm}^{-1}$ )	$m_n^c$ ( $\text{nm}^{-2}$ )	$g_{r,\text{eff}}^{\uparrow\downarrow}$ ( $\text{nm}^{-2}$ )	$\alpha_R$ (eV-pm)	$v_F$ ( $\times 10^6 \text{ ms}^{-1}$ )	$p'_{0,\text{eff}}$	$ \zeta_{\text{SOT}} $ [from Eq. (19)]	$ \zeta_{\text{SOT}} $ (measured)
Au   FM	5.9 <sup>a</sup> [46]	12	23	2.7 [68]	39.6 [74]	1.38 [50]	0.044	0.0033	0.0033 [75] 0.0035 [10,76]
Cu   Bi   Ni-Fe	8.47 <sup>a</sup> [46]	13.6	29.4	10.1 [77]	320 [48]	1.57 <sup>a</sup> [46]	0.296	0.07	0.24 <sup>d</sup> [17]
Ag   Bi   Ni-Fe	5.86 <sup>a</sup> [46]	12	22.98	32.1 [78]	56 [74]	1.39 <sup>a</sup> [46]	0.06	0.053	0.023 [18]
STO   LAO   Ni-Fe	—	1.28 <sup>b</sup>	0.26	13.3 [20]	3 [20]	0.074 <sup>c</sup>	0.062	2	1.8 [21]

<sup>a</sup>Parameters taken for the most conductive layer in the system.

<sup>b</sup>Estimated using  $k_F = \sqrt{2\pi n_s}$  with  $n_s = 2.6 \times 10^{17} \text{ m}^{-2}$  [20].

<sup>c</sup>Estimated using  $v_F = \hbar k_F / m^*$  with  $m^* = 2m_0$  [20].

<sup>d</sup>This value was measured on a CuBi alloy, not on a Cu | Bi bilayer.

<sup>e</sup>Calculated using Eq. (4a).

estimated from the Cu|Bi Rashba interface is of the same order as values observed in Au|FM, and Ag|Bi|Ni-Fe. We note that the estimation of  $\zeta_{\text{SOT}}$  for a Cu|Bi interface is 3 times lower than the experimental observation on CuBi alloy, which indicates that such an alloy has a different origin of SML, e.g., the resonant scattering from the Bi impurities, as discussed in Ref. [17]. Such scattering-induced charge-spin interconversion is included in our general model and arises due to  $p_{rs}$  as described in Sec. II B and Appendix A.

### 3. SOT efficiencies in oxides

Recently, there is an increasing interest in transition metal oxides (see, e.g., Refs. [20–23]) for tunable charge-spin interconversion. In the semimetallic phase of strontium iridate ( $\text{SrIrO}_3$ ), it has been observed that  $\zeta_{\text{SOT}}$  increases for thicker devices while  $\rho$  of the sample decreases [22,23], see Fig. 4(a). This observation is counterintuitive to the observations in metals [59] where higher resistivity exhibits higher SOT efficiency. Interestingly, the Hall carrier concentration measured on bare  $\text{SrIrO}_3$  [22] indicated that the concentration is also decreasing for thicker samples [see Fig. 4(a)]. A similar observation that the resistivity and carrier concentration scale in the same direction with thickness has previously been observed in  $\text{Bi}_2\text{Se}_3$  [63] and  $\text{Bi}_2\text{Te}_3$  [64].

Equation (20) indicates a scaling trend that  $\zeta_{\text{SOT}} \propto n^{-(2/3)}$ . We calculate the SOT efficiency using Eq. (20) from the measured  $n$  with varying sample thickness [see Fig. 4(a)] and compare it with the SOT efficiency measurements on  $\text{SrIrO}_3$  reported in Ref. [23], as shown in Fig. 4(b). We set  $p'_{0,\text{eff}} g_{r,\text{eff}}^{\uparrow\downarrow} \approx 1.9 \times 10^{18} \text{ m}^{-2}$  to match the absolute value of  $\zeta_{\text{SOT}}$  and assume it to be constant over various thicknesses. The assumption that  $g_{r,\text{eff}}^{\uparrow\downarrow}$  is constant over various thicknesses is based on the experimental observation in Ref. [23]. It is surprising to note that two features observed in the SOT measurements are captured in the calculations using Eq. (20).

1. Independently measured  $n$  decreases with thickness, and saturates for thicker samples [see Fig. 4(a)]. Based on this observation, Eq. (20) indicates that the SOT efficiency will increase with the thickness and will saturate around the same thickness where  $n$  saturates. Interestingly, the calculated  $\zeta_{\text{SOT}}$  using Eq. (20) shows good agreement with the measurements reported in Ref. [23].

2. The measured change in the SOT efficiency [ $\Delta\zeta_{\text{SOT}}$  in Fig. 4(b)] between the thin and the thick limits is roughly the same as the value calculated using the change in  $n$ .

The origin of the carrier-concentration change with thickness needs a careful evaluation in the future and could arise from a phase change from tetragonal to orthorhombic [23], or a change in strain in the system [65]. It has been discussed in the past [65] that a strain on  $\text{SrIrO}_3$  can significantly modulate the carrier concentration, i.e., the density of states in the material, which could be a promising way to achieve high  $\zeta_{\text{SOT}}$  in an oxide system. Interestingly, such a strain-induced tunability in the inverse voltage has been shown recently [66].

### 4. Model parameters for $\zeta_{\text{SOT}} > 1$

In several of our calculations, we find  $\zeta_{\text{SOT}} > 1$  using parameters reported in the literature. For example, the  $\Delta R_s$  for  $\text{Bi}_2\text{Se}_3$  (in Table I) multiplied by the reported  $g_{r,\text{eff}}^{\uparrow\downarrow}$  gives a calculated SOT efficiency  $\zeta_{\text{SOT}} > 1$ , and similar high values have been observed experimentally (see, e.g., Refs. [37,72]). Also, the  $\zeta_{\text{SOT}}$  estimated for the LAO|STO Rashba interface using Eq. (19) is  $> 1$  and in agreement with the experimental observation in Ref. [21], see Table IV. Note that  $p'_{0,\text{eff}} \approx 0.062$  in LAO|STO and  $\zeta_{\text{SOT}} > 1$  arises due to  $g_{r,\text{eff}}^{\uparrow\downarrow} \gg m_n$  in Eq. (19). Also, the calculated  $\zeta_{\text{SOT}}$  is  $> 1$  for  $\text{WTe}_2$ ; however, the existing experimental report on  $\text{WTe}_2$  is  $< 1$  (see, Ref. [73]). We note that, for a proper estimation, the spin-mixing conductance should be taken carefully since the reported values can be overestimated due to various nonideal effects [79]. A more detailed analysis of Eq. (19) for the cases where  $\zeta_{\text{SOT}} > 1$  we leave

for the future when more data are available as the field evolves.

## D. Comparison with conventional view

### 1. Effective SOT efficiency

According to the semiclassical model in Ref. [36], the SOT efficiency is given by [12]

$$\zeta_{\text{SOT}} = \theta_{\text{SH}} \frac{g_r^{\uparrow\downarrow}}{g_r^{\uparrow\downarrow} + g'_{\text{so}}} \tanh \frac{t}{2\lambda_{\text{sd}}} \tanh \frac{t}{\lambda_{\text{sd}}}, \quad (21)$$

where  $\theta_{\text{SH}}$  is the internal spin Hall angle,  $\lambda_{\text{sd}}$  is the spin-diffusion length,  $g_r^{\uparrow\downarrow}$  is the real part of the bare spin-mixing conductance and  $(q^2/h)g'_{\text{so}} = (\sigma/2\lambda_{\text{sd}}) \tanh(t/\lambda_{\text{sd}})$ . In the thick SO layer limit ( $t \gg \lambda_{\text{sd}}$ ) and in the high resistivity SO layer limit ( $g'_{\text{so}} \ll g_r^{\uparrow\downarrow}$ ), we have

$$\zeta_{\text{SOT}} \approx \theta_{\text{SH}}. \quad (22)$$

Equation (19) shows a similar dependence on  $g_{r,\text{eff}}^{\uparrow\downarrow} = g_r^{\uparrow\downarrow} g_{\text{so}} / (g_r^{\uparrow\downarrow} + g_{\text{so}})$  where this term is determined by  $\min(g_r^{\uparrow\downarrow}, g_{\text{so}})$ . In the limit where  $g_{\text{so}} \ll g_r^{\uparrow\downarrow}$  and weak  $p'_{0,\text{eff}}$  reduces to

$$\zeta_{\text{SOT}} \approx \alpha p'_{0,\text{eff}} \times \frac{g_{\text{so}}}{m_n}, \quad (23)$$

where  $(2q^2/h)g_{\text{so}}L_f w_f = G_{\text{so}}$  is given by Eq. (8). Note that in this limit, Eq. (23) is determined completely by the SO layer parameters.

Note that the limit  $g_{\text{so}} \ll g_r^{\uparrow\downarrow}$  do not represent highly resistive channel within our model. When the SO layer has strong SML, even in the high-resistivity limit we can satisfy  $g_{\text{so}} \gg g_r^{\uparrow\downarrow}$  since  $g_{\text{so}} \propto 1/(1 - p_0^2)$ , which yields

$$\zeta_{\text{SOT}} \approx \alpha p'_{0,\text{eff}} \times \frac{g_r^{\uparrow\downarrow}}{m_n}. \quad (24)$$

### 2. Internal spin Hall angle

We can define an internal spin Hall angle in the weak SML limit from Eq. (23), as

$$\theta_{\text{SH}} \equiv \alpha p'_{0,\text{eff}} \times \frac{g_{\text{so}}}{m_n}.$$

The internal spin Hall angle is often defined in terms of a spin Hall conductivity  $\sigma_{\text{SH}}$  as

$$\theta_{\text{SH}} = \frac{\sigma_{\text{SH}}}{\sigma}. \quad (25)$$

Noting that  $\sigma = (q^2/h)m_n\lambda_m$ , we can also define a spin Hall conductivity from Eq. (23) as

$$\sigma_{\text{SH}} = 2G'_{\text{so}}\lambda_{\text{IREE}}, \quad (26)$$

where  $G'_{\text{so}} = G_{\text{so}}/(w_f L_f)$ . The model described in this paper considers transport near the Fermi energy and describes  $\sigma_{\text{SH}}$  in terms of material density of states, degree of SML, mean free path, and spin source conductance. However, the conventional approach calculates  $\sigma_{\text{SH}}$  using spin Berry phase from the electronic band structure and by taking into account contributions from anomalous velocities from all of the occupied states in the conduction band [60,61], including the states well below the Fermi energy. In the disordered phase of the material, Bloch state description is not well defined; however, the density of states and the number of modes are well defined and measurable, even within a highly disordered sample.

## IV. INVERSE EFFECT: SPIN-TO-CHARGE CONVERSION

### A. Spin current to charge voltage

A spin current  $i_s$  injected into the SO layer from a FM layer will induce an open-circuit charge voltage across the sample [see Fig. 1(a)] as given by

$$V_{12} = -\frac{\alpha \xi p_{0,\text{eff}}}{2G_B} i_s, \quad (27)$$

where the spin current  $i_s$  can be generated in various ways, e.g., spin pumping [20,78,80,81], spin Seebeck effect [82,83], and electrical injection through a ferromagnetic contact [6,31,33]. Eq. (27) satisfies the Onsager relation with Eq. (11) (see Ref. [40]).

The Onsager reciprocity [40,94] requires that in Fig. 1(a), we have

$$\frac{V_{32}(\vec{m})}{I_{12}} = \frac{V_{12}(-\vec{m})}{I_{32}}, \quad (28)$$

which in conjunction with Eq. (12) gives a reciprocal effect, given by

$$V_{12}(+\vec{m}) - V_{12}(-\vec{m}) = -\frac{\alpha \xi p_{0,\text{eff}} p_f}{G_B} I_{32}. \quad (29)$$

Equation (29) represents the inverse effect by electrical injection of a spin current  $i_s \approx p_f I_{32}$  by flowing a current through the FM contact. Noting that  $V_{12}(+\vec{m}) - V_{12}(-\vec{m}) \equiv 2V_{12}$ , we get the Eq. (27). The strength of the spin current induced charge voltage is the same as the charge-current-induced spin voltage and determined by the charge-spin interconversion resistance  $\Delta R_s$  shown in Fig. 2(b), but differs by a negative sign. According to Eq. (28), we can write

$$\Delta R_s = \frac{V_{32}(+\vec{m}) - V_{32}(-\vec{m})}{I_{12}} = -\frac{V_{12}(+\vec{m}) - V_{12}(-\vec{m})}{I_{32}}.$$

Thus, the spin-current-induced charge voltage should show an inverse relation with the density of states of SO

TABLE V. Inverse Rashba-Edelstein effect (IREE) length in diverse materials.

Material	$\lambda_m$ (nm)	$p'_{0,\text{eff}}$	$\lambda_{\text{IREE}}$ (nm) [Eq. (32)]	$\lambda_{\text{IREE}}$ (nm) (measured)
Ag Bi	22.6	0.06	0.43	0.3 [78]
Cu Bi	0.88	0.054	0.015	0.009 [33]
Ag Bi <sub>2</sub> O <sub>3</sub>	53.3	0.017	0.28	0.15 ± 0.03 [84]
Cu Bi <sub>2</sub> O <sub>3</sub>	39.9	0.024	0.3	0.17 ± 0.03 [84]
Au Bi <sub>2</sub> O <sub>3</sub>	37.7	0.011	0.13	0.09 ± 0.03 [84]
Al Bi <sub>2</sub> O <sub>3</sub>	18.9	0.004	0.024	0.01 ± 0.002 [84]
Fe Ge(111)	3.27	0.11	0.12	0.13 [85]
MoS <sub>2</sub>  Al	40	0.3	3.82	4 [86]
LAO STO	180.4	0.062	3.56	6.4 [20]
Bi <sub>2</sub> Se <sub>3</sub>	6.26	0.066	0.13	0.035 [87]
		0.12	0.24	0.32 [88]
		0.88	1.75	

$\lambda_m$  and  $p'_{0,\text{eff}}$  estimations are summarized in Table VI.

material. It has been recently shown that the inverse spin Hall voltage in VO<sub>2</sub> exhibits an incremental jump while transitioning from metal to insulator phase [95]. This observation is in agreement with Eq. (27) since it is well known that the Hall carrier concentration in VO<sub>2</sub> shows a jump across the transition point [96].

## B. Spin current to charge current

The inverse effect in 2D channels with SML are often quantified with the following figure of merit:

$$\lambda_{\text{IREE}} = \frac{J_c}{J_s}, \quad (30)$$

known as the inverse Rashba-Edelstein effect length. Here  $J_c$  is the charge current density in the 2D channel (unit, A m<sup>-1</sup>) induced by the injected spin current density  $J_s$  (unit, A m<sup>-2</sup>).

From Fig. 1, if we connect terminals 1 and 2, the short-circuit charge current,  $I_{\text{SC}}$ , for a given spin current ( $i_s$ ) injection is given by

$$I_{\text{SC}} = \frac{G_B \lambda_m}{\lambda_m + L} \times \frac{\alpha p'_{0,\text{eff}} i_s}{2G_B}. \quad (31)$$

For a diffusive channel ( $L \gg \lambda_m$ ), we obtain an expression for  $\lambda_{\text{IREE}}$ , as given by

$$\lambda_{\text{IREE}} = \frac{I_{\text{SC}}/w}{i_s/(wL)} = \frac{p'_{0,\text{eff}} \lambda_m}{\pi}. \quad (32)$$

Here, we compare Eq. (32) with available experiments on diverse classes of materials: Ag|Bi [78], Cu|Bi [33],

TABLE VI. Mean free path ( $\lambda_m$ ) and effective degree of spin-momentum locking ( $p'_{0,\text{eff}}$ ) in diverse materials.

SOC material	$w$ ( $\mu\text{m}$ )	$t$ (nm)	$k_F$ (nm <sup>-1</sup> )	$G_B$	$R$ ( $\Omega$ )	$R_{\text{sheet}}$ ( $\Omega/\square$ )	$\rho$ ( $\mu\Omega\text{ cm}$ )	$\lambda_m$ (nm)	$\alpha_R$ (eV Å)	$v_F$ ( $\times 10^6\text{ m s}^{-1}$ )	$p'_{0,\text{eff}}$
Ag Bi	400 [78]	5 [78]	12	1.77 kS	—	10 <sup>a</sup>	—	22.6	0.56 [78]	1.39 [46]	0.06
Cu Bi	0.15 [33]	20 [33]	13.6	3.4 S	—	—	100 <sup>g</sup>	0.88	0.56 [33]	1.57 [46]	0.054
Ag Bi <sub>2</sub> O <sub>3</sub>	—	—	—	—	—	—	—	53.3 [50]	0.16 [84]	1.39 [46]	0.017
Cu Bi <sub>2</sub> O <sub>3</sub>	—	—	—	—	—	—	—	39.9 [50]	0.25 [84]	1.57 [46]	0.024
Au Bi <sub>2</sub> O <sub>3</sub>	—	—	—	—	—	—	—	37.7 [50]	0.1 [84]	1.4 [46]	0.011
Al Bi <sub>2</sub> O <sub>3</sub>	—	—	—	—	—	—	—	18.9 [50]	0.055 [84]	2.03 [46]	0.004
Fe Ge(111)	400 [85]	20 <sup>d</sup> [85]	17.1 <sup>c</sup>	14.4 kS	51 [85]	—	—	3.27 <sup>f</sup>	1.5 [89] <sup>b</sup>	1.98 <sup>c</sup> [46]	0.11
MoS <sub>2</sub>  Al	—	—	—	—	—	—	—	40 [90]	1.097 [91]	0.53 [92]	0.3
LAO STO	400 [20]	—	1.28	12.6 S	—	176 <sup>h</sup>	—	180.4	0.03 [20]	0.074 <sup>i</sup> [20]	0.062
Bi <sub>2</sub> Se <sub>3</sub>	1000 [87]	9 [87]	1.14	71.92 S	—	—	2000 <sup>j</sup>	6.26	—	—	0.066 <sup>k</sup> 0.12 <sup>k</sup> 0.88 <sup>k</sup>

<sup>a</sup>Corresponds to sample with 5-nm Ag in Ref. [78].

<sup>b</sup>Estimated for the Ge interface with a metal, which is higher than that reported for strained bulk Ge [93].

<sup>c</sup>The Fermi velocity of the conductive layer Fe.

<sup>d</sup>Thickness of the most conducting layer is taken for calculation.

<sup>e</sup>Calculated using  $k_F = (3\pi^2 n)^{1/3}$  from electron density of Fe:  $n = 1.7 \times 10^{29}\text{ m}^{-3}$  [46].

<sup>f</sup>Estimated from  $R = L/(G_B \lambda_m)$  with length  $L = 2.4\text{ mm}$  [85].

<sup>g</sup> $\rho$  of the Bi layer is used, which is taken from Ref. [33].

<sup>h</sup>Taken from Fig. 1(d) of Ref. [20] for LAO|STO at 7 K.

<sup>i</sup>We estimate the Fermi velocity using  $v_F = (\hbar k_F/m^*)$ .  $m^* \approx 2 \times 9.1 \times 10^{-31}\text{ kg}$  as reported in Ref. [20].

<sup>j</sup>Taken from Fig. 2(b) of Ref. [87] at approximately 300 K.

<sup>k</sup>Taken from Table II.

Ag|Bi<sub>2</sub>O<sub>3</sub> [84], Cu|Bi<sub>2</sub>O<sub>3</sub> [84], Au|Bi<sub>2</sub>O<sub>3</sub> [84], Al|Bi<sub>2</sub>O<sub>3</sub> [84], LaAlO<sub>3</sub>|SrTiO<sub>3</sub> (LAO|STO) [20], Bi<sub>2</sub>Se<sub>3</sub> [87], Fe/Ge(111) [85], and MoS<sub>2</sub> [86,97], which show good agreement as shown in Fig. 5. The estimations are summarized in Table V. Note that the figure of merit in Eq. (32) do not depend on the material density of states, but depend on the mean free path of the sample. One interesting observation in Table V is that the  $p'_{0,\text{eff}}$  in the LAO|STO Rashba channel is weak. The large  $\lambda_{\text{IREE}}$  observed in Ref. [20] is due to a large mean free path of the channel.

## V. SUMMARY

The physics of charge-spin interconversion in various spin-orbit materials is a topic of great current interest for modern spintronics. Over the past decade, many materials have been studied, e.g., topological insulators, transition metals, Kondo insulators, semimetals, semiconductors, and oxides, to enhance interconversion efficiency. In this paper, we discuss a unified theoretical framework for such materials that relate the interconversion efficiency to the fundamental material parameters. We show that the charge-spin interconversion efficiency scales inversely with the channel number of modes or the material density of states near the Fermi energy. We further discuss two widely used figure of merits: SOT efficiency and inverse Rashba-Edelstein effect length for diverse classes of materials and how to enhance them in terms of materials and device parameters. Remarkably, experimental data obtained over the last decade on different materials closely follow our theoretical model which provides a unifying conceptual framework. We point out a scaling trend of the SOT efficiency with respect to the carrier concentration in agreement with the experiments. This unified model will enable a roadmap for materials with spin-orbit coupling and help design appropriate material systems and devices for desired spintronic applications.

## ACKNOWLEDGMENTS

This work is supported by Applications and Systems-driven Center for Energy-Efficient integrated Nano Technologies (ASCENT), one of six centers in Joint University Microelectronics Program (JUMP), a Semiconductor Research Corporation (SRC) program sponsored by Defense Advanced Research Projects Agency (DARPA). S. Hong acknowledges support from the National Research and Development Program through the National Research Foundation of Korea (NRF), funded by the Ministry of Science and ICT (2019M3F3A1A02071509 and 2020M3F3A2A01081635) and KIST institutional program (2E31032). The authors are thankful to Professor Daniel C. Ralph in Cornell University, for the insightful discussions on the spin-orbit torque efficiencies in diverse classes of materials.

## APPENDIX A: RESISTANCE MODEL AND CIRCUIT REPRESENTATION

In this section, we derive Eq. (1) from the semiclassical equations in Ref. [28].

### 1. Semiclassical model

#### a. Diffusion equation for a SML channel

We start from the diffusion equations for a general channel with spin-momentum locking [28], as given by

$$\begin{aligned} \frac{d}{dx} I_c &= i^c, \\ \frac{d}{dx} V_c &= - \left( \frac{1}{\lambda} + \frac{1}{\lambda_B} \right) \frac{I_c}{G_B} - \frac{\alpha p_f}{\lambda_B G_B} I_s \\ &\quad + \frac{2}{\alpha} \left( \frac{1}{\lambda'} + \frac{p_0}{\lambda_B} \right) V_s + \frac{2p_0 p_f}{\lambda_B} V_c + \frac{\alpha p_0}{2G_B} i^s, \\ \frac{d}{dx} I_s &= - \frac{4G_B}{\alpha^2 \lambda_s} V_s + \frac{2}{\alpha \lambda'_s} I_c + i^s, \quad \text{and} \\ \frac{d}{dx} V_s &= - \frac{\alpha^2}{G_B} \left( \frac{1}{\lambda_0} + \frac{1}{\lambda_B} \right) I_s - \frac{\alpha p_f}{\lambda_B G_B} I_c \\ &\quad + 2\alpha p_0 \left( \frac{1}{\lambda_0} + \frac{1}{\lambda_B} \right) V_c + \frac{2p_0 p_f}{\lambda_B} V_s + \frac{\alpha p_0}{2G_B} i^c. \end{aligned} \quad (\text{A1})$$

Equation (A1) is obtained by combining Eqs. (8), (9), and (62) in Ref. [28], which were obtained from Boltzmann transport equation by classifying electronic states in the channel into four groups, based on their spin-polarization index (up or down) and the sign of the group velocity (positive or negative), see Fig. 6. Here,  $I_c$ ,  $I_s$  are charge and spin currents in the channel,  $V_c$ ,  $V_s$  are charge and spin voltages in the channel,  $G_B$  is given by Eq. (3),  $p_0$  is given by Eq. (5), and  $\alpha$  is an angular averaging factor.  $i^c$ ,  $i^s$  are charge and spin current per unit length entering into the channel from an external contact with conductance per unit length  $G_0$  and contact polarization  $p_f$ . The scattering length  $\lambda_B$  in Eq. (A1) is determined by the conductance of the external contact with respect to the channel number of modes, as given by

$$\frac{1}{\lambda_B} = \frac{G_0}{4G_B}, \quad (\text{A2})$$

where  $G_0$  is the contact conductance per unit length of the contact.  $\lambda$ ,  $\lambda_0$ ,  $\lambda_s$ ,  $\lambda'$ , and  $\lambda'_s$  are scattering lengths in the channel, which are described below.

#### b. Scattering lengths in the channel

We consider three types of scattering processes among the four groups of electronic states in the channel as shown in Fig. 6:

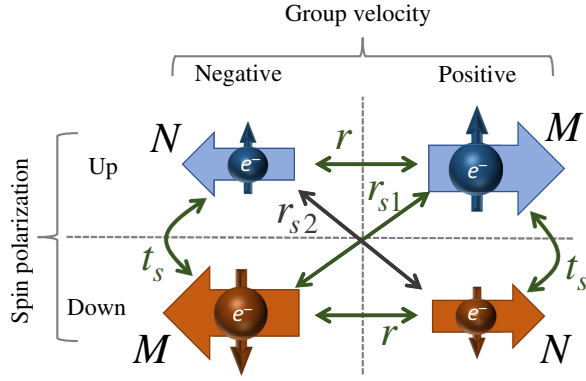


FIG. 6. Scattering mechanisms considered in the formalism among the four groups of electronic states, classified according to the spin-polarization index (up or down) and the sign of the group velocity (positive or negative).

1. transmission with spin flip with scattering rate  $t_s$ ;
2. reflection without spin flip with scattering rate  $r$ ; and
3. reflection with spin flip. Forward moving up spins become backward moving down spins and vice versa within the  $M$  modes, with a scattering rate  $r_{s1}$ . Similarly, forward moving down spins become backward moving up spins and vice versa within the  $N$  modes, with a scattering rate  $r_{s2}$ .

Here, the scattering rates  $r$ ,  $t_s$ ,  $r_{s1,2}$  are in the units of per unit length. The scattering lengths  $\lambda$ ,  $\lambda_0$ , and  $\lambda_s$  in Eq. (A1) are given by [28]

$$\begin{aligned} \frac{1}{\lambda} &= \frac{1}{2} \left( \frac{r_{s2}}{N} + \frac{r_{s1}}{M} \right) + \frac{r}{2} \left( \frac{1}{N} + \frac{1}{M} \right), \\ \frac{1}{\lambda_0} &= \frac{r + t_s}{2} \left( \frac{1}{N} + \frac{1}{M} \right), \text{ and} \\ \frac{1}{\lambda_s} &= \frac{1}{2} \left( \frac{r_{s2}}{N} + \frac{r_{s1}}{M} \right) + \frac{t_s}{2} \left( \frac{1}{N} + \frac{1}{M} \right). \end{aligned} \quad (\text{A3})$$

Here,  $\lambda$  is the back-scattering length for the charge transport,  $\lambda_0$  is a scattering length for the spin transport, and  $\lambda_s$  is a scattering length for spin relaxation in the channel. The scattering lengths  $\lambda'$  and  $\lambda'_s$  in Eq. (A1) are related to spin-induced charge and charge-induced spin, respectively. They are given by [28]

$$\begin{aligned} \frac{1}{\lambda'} &= \frac{1}{2} \left( \frac{r_{s2}}{N} - \frac{r_{s1}}{M} \right) + \frac{r}{2} \left( \frac{1}{N} - \frac{1}{M} \right), \text{ and} \\ \frac{1}{\lambda'_s} &= \frac{1}{2} \left( \frac{r_{s2}}{N} - \frac{r_{s1}}{M} \right) + \frac{t_s}{2} \left( \frac{1}{N} - \frac{1}{M} \right). \end{aligned} \quad (\text{A4})$$

For simplicity of the analytical details, we define

$$\begin{aligned} \frac{1}{\lambda_r} &= \frac{r}{2} \left( \frac{1}{N} + \frac{1}{M} \right), \\ \frac{1}{\lambda_t} &= \frac{t_s}{2} \left( \frac{1}{N} + \frac{1}{M} \right), \text{ and} \\ \frac{1}{\lambda_{rs}} &= \frac{1}{2} \left( \frac{r_{s2}}{N} - \frac{r_{s1}}{M} \right), \end{aligned} \quad (\text{A5})$$

which allows us to rewrite Eq. (A4) as

$$\begin{aligned} \frac{1}{\lambda'} &= \frac{1}{\lambda_{rs}} + \frac{p_0}{\lambda_r}, \text{ and} \\ \frac{1}{\lambda'_s} &= \frac{1}{\lambda_{rs}} + \frac{p_0}{\lambda_t}. \end{aligned} \quad (\text{A6})$$

Note that the resistance matrix similar to Eq. (1) presented in Ref. [28] considered potentiometric (noninvasive) external contacts only, by assuming  $\lambda_B \rightarrow \infty$ . Also, to derive the resistance matrix, Ref. [28] assumed that the spin-flip reflection is the dominant scattering, i.e.  $(1/\lambda), (1/\lambda_s) \gg (1/\lambda_0), (1/\lambda'), (1/\lambda'_s)$ . In this paper, we present a resistance matrix applicable for general scattering conditions and contacts with arbitrary conductance.

## 2. Assumptions

We make the following two assumptions:

(a) No charge current is flowing out of the external contact, i.e.,  $i^c = 0$ . The external contact can only inject or absorb a spin current  $i^s$ .

(b) We consider a channel region where the spin voltage is uniform, i.e.,

$$\frac{d}{dx} V_s = 0.$$

Thus the diffusion equations can be rewritten as

$$\frac{d}{dx} I_c = 0, \quad (\text{A7a})$$

$$\begin{aligned} \frac{d}{dx} V_c &= - \left( \frac{1}{\lambda} + \frac{1}{\lambda_B} \right) \frac{I_c}{G_B} - \frac{\alpha p_f}{G_B \lambda_B} I_s \\ &+ \frac{2}{\alpha \lambda_{rs}} V_s + \frac{2p_0}{\alpha} \left( \frac{1}{\lambda_r} + \frac{1}{\lambda_B} \right) V_s + \frac{2p_0 p_f}{\lambda_B} V_c + \frac{\alpha p_0}{2G_B} i^s, \end{aligned} \quad (\text{A7b})$$

$$\frac{d}{dx} I_s = - \frac{4G_B}{\alpha^2 \lambda_s} V_s + \frac{2}{\alpha \lambda_{rs}} I_c + \frac{2p_0}{\alpha \lambda_t} I_c + i^s, \text{ and} \quad (\text{A7c})$$

$$\begin{aligned} \frac{d}{dx}V_s = 0 = & -\frac{\alpha^2}{G_B} \left( \frac{1}{\lambda_0} + \frac{1}{\lambda_B} \right) I_s \\ & - \frac{\alpha p_f}{\lambda_B G_B} I_c + 2\alpha p_0 \left( \frac{1}{\lambda_0} + \frac{1}{\lambda_B} \right) V_c + \frac{2p_0 p_f}{\lambda_B} V_s. \end{aligned} \quad (\text{A7d})$$

Equation (A7d) can be simplified as

$$I_s = \frac{2p_0 G_B}{\alpha} V_c - \frac{\kappa p_f}{\alpha} I_c + \frac{\kappa p_f}{\alpha} \frac{2p_0 G_B}{\alpha} V_s, \quad (\text{A8})$$

where

$$\kappa = \frac{\lambda_0}{\lambda_0 + \lambda_B}. \quad (\text{A9})$$

### 3. Second row of the resistance matrix

We differentiate both sides of Eq. (A8) with respect to  $x$  and combine with Eqs. (A7a) and (A7d) to get

$$\frac{d}{dx}I_s = \frac{2p_0 G_B}{\alpha} \frac{d}{dx}V_c, \quad (\text{A10})$$

which we further combine with Eqs. (A7b) and (A7c) to get

$$\begin{aligned} -\frac{4G_B}{\alpha^2} \left[ \frac{1}{\lambda_s} + p_0 \left( \frac{1}{\lambda_{rs}} + \frac{p_0}{\lambda_r} + \frac{p_0}{\lambda_B} \right) \right] V_s = & -\frac{2p_0 p_f}{\lambda_B} I_s \\ -\frac{2}{\alpha} \left[ \frac{1}{\lambda_{rs}} + p_0 \left( \frac{1}{\lambda_t} + \frac{1}{\lambda} + \frac{1}{\lambda_B} \right) \right] I_c = & \\ + \frac{4p_0^2 p_f G_B}{\alpha \lambda_B} V_c - (1 - p_0^2) i^s, \end{aligned} \quad (\text{A11})$$

We then combine Eqs. (A11) and (A8) to get

$$V_s = \frac{\alpha \lambda_{s0}}{2G_B \lambda_{rs}} I_c + \frac{\alpha \epsilon p_0}{2G_B} I_c + \frac{\alpha^2 (1 - p_0^2) \lambda_{s0}}{4G_B L} i_s, \quad (\text{A12})$$

where  $i_s = Li^s$ ,  $\lambda_{s0}$ , and  $\epsilon$  are given by

$$\frac{1}{\lambda_{s0}} = \frac{1}{\lambda_s} + \frac{p_0^2}{\lambda_r} + \frac{p_0^2}{\lambda_B} (1 - \kappa p_f^2), \quad \text{and} \quad (\text{A13a})$$

$$\epsilon = \frac{\lambda_{s0}}{\lambda_t} + \frac{\lambda_{s0}}{\lambda} + \frac{\lambda_{s0}}{\lambda_B} (1 - \kappa p_f^2). \quad (\text{A13b})$$

### 4. First row of the resistance matrix

We combine Eq. (A7b) with Eq. (A8) to get

$$\begin{aligned} \frac{d}{dx}V_c = & -\left( \frac{1}{\lambda} + \frac{1 - \kappa p_f^2}{\lambda_B} \right) \frac{I_c}{G_B} + \frac{2}{\alpha \lambda_{rs}} V_s \\ & + \frac{2p_0}{\alpha} \left( \frac{1}{\lambda_r} + \frac{1 - \kappa p_f^2}{\lambda_B} \right) V_s + \frac{\alpha p_0}{2G_B} i^s. \end{aligned} \quad (\text{A14})$$

We apply  $dV_c/dx = -(V_1 - V_2)/L$  and combine Eq. (A14) with Eq. (A12) to get

$$\begin{aligned} V_1 - V_2 = & \frac{L}{G_B \lambda_m} I_c - \frac{\alpha p_0}{2G_B} \left\{ \frac{\lambda_{s0}}{\lambda_r} + \frac{\lambda_{s0}}{\lambda_s} + \frac{\lambda_{s0}}{\lambda_B} (1 - \kappa p_f^2) \right\} i_s \\ & - \frac{\alpha \lambda_{s0}}{2G_B \lambda_{rs}} i_s, \end{aligned} \quad (\text{A15})$$

where  $i_s = Li^s$  and the effective mean free path ( $\lambda_m$ ) is given by

$$\begin{aligned} \frac{1}{\lambda_m} = & \frac{1}{\lambda} - \frac{p_0^2}{\lambda_r} - \frac{\lambda_{s0}}{\lambda_{rs}^2} - \frac{p_0}{\lambda_{rs}} - \frac{p_0 \lambda_{s0}}{\lambda_r \lambda_{rs}} \\ & + \frac{1 - \kappa p_f^2}{\lambda_B} \left( \frac{\lambda_{s0}}{\lambda_s} + \frac{\lambda_{s0} p_0^2}{\lambda_r} - \frac{\lambda_{s0} p_0^2}{\lambda_t} - \frac{\lambda_{s0} p_0^2}{\lambda} \right). \end{aligned} \quad (\text{A16})$$

From Eqs. (A3) and (A4) we see that

$$\frac{1}{\lambda} + \frac{1}{\lambda_t} = \frac{1}{\lambda_s} + \frac{1}{\lambda_r}, \quad (\text{A17})$$

which allows us to write Eq. (A15) as

$$V_1 - V_2 = \frac{L}{G_B \lambda_m} I_c - \frac{\alpha \epsilon p_0}{2G_B} i_s - \frac{\alpha \lambda_{s0}}{2G_B \lambda_{rs}} i_s. \quad (\text{A18})$$

The terms related to  $\lambda_{rs}$  in Eqs. (A18) and (A12) indicate an additional component on charge-spin interconversion induced by spin-flip scatterings. We define the strength of such scattering-induced charge-spin interconversion as

$$p_{rs} = \frac{\lambda_{s0}}{\lambda_{rs}}. \quad (\text{A19})$$

Thus we can write Eqs. (A18) and (A12) as

$$\begin{aligned} V_1 - V_2 = & \frac{L}{G_B \lambda_m} I_c - \frac{\alpha p_{0,\text{eff}}}{2G_B} i_s, \\ V_s = & \frac{\alpha p_{0,\text{eff}}}{2G_B} I_c + \frac{\alpha^2 (1 - p_0^2) \lambda_{s0}}{4G_B L} i_s, \end{aligned}$$

which yields the resistance matrix in Eq. (1), where  $p_{0,\text{eff}}$  is given by

$$p_{0,\text{eff}} = \epsilon p_0 + p_{rs}, \quad (\text{A20})$$

which indicate that the charge-spin interconversion can have a contribution from the band structure of the material

(given by  $p_0$ ) and also a spin-dependent-scattering-induced component (given by  $p_{rs}$ ).

### 5. Pure scattering-induced charge-spin interconversion

Equations (A18) and (A12) indicate a pure scattering-induced charge-spin interconversion, even in a normal metal (i.e.,  $p_0 = 0$  or  $M = N$ ). Such charge-spin interconversion can be induced in a normal metal due to a difference in  $r_{s1}$  and  $r_{s2}$ , i.e., forward (or backward) moving up spins scatter at a different rate than the down spins. In a normal metal, Eqs. (A18) and (A12) become

$$V_1 - V_2 = \frac{L}{G_B \lambda'_m} I_c - \frac{\alpha p_{rs}}{2G_B} i_s. \quad (\text{A21a})$$

$$V_s = \frac{\alpha p_{rs}}{2G_B} I_c + \frac{\alpha^2 \lambda_s}{4G_B L} i_s, \quad (\text{A21b})$$

where  $(1/\lambda'_m) = (1/\lambda) + (\lambda_s/\lambda_{rs}^2)$ , and  $p_{rs}$  represents the strength of the spin-flip scattering induced charge-spin interconversion in a normal metal channel, given by

$$p_{rs} = \frac{(r_{s2} + ts) - (r_{s1} + ts)}{(r_{s2} + ts) + (r_{s1} + ts)}. \quad (\text{A22})$$

Equations (A21a)–(A21b) indicate a charge-to-spin and a spin-to-charge conversion in a normal metal channel, similar to Eq. (1) describing a SML channel.

The phenomena described by Eqs. (A21a)–(A21b) are aligned with experimental observations on impurity scattering-induced high SOT (e.g., Ref. [17]), where a copper sample (a well-known normal metal channel) exhibits a large SOT by introducing bismuth impurities. Note that, in the present paper, we extract  $p'_{0,\text{eff}}$  from measurements and do not assume any particular origin.

### APPENDIX B: NUMBER OF MODES AND DENSITY OF STATES

The density of states in a material is given by

$$D_0 = \frac{dN}{dE} = \frac{dN}{dp} \frac{dp}{dE}, \quad (\text{B1})$$

where  $N$  is the number of electronic states in the channel,  $p$  is the momentum, and  $E$  is the energy. Noting that the group velocity  $v = dE/dp$ , Eq. (B1) gives

$$D_0 v = \frac{dN}{dp}. \quad (\text{B2})$$

The total number of states,  $N(p)$ , that have a momentum less than  $p$  can be counted using the following formula for

a 2D channel with length  $L$  and width  $w$  [29]

$$N(p) = 2 \times \frac{\pi p^2}{\frac{h}{L} \frac{h}{w}}, \quad (\text{B3})$$

and using the following formula for a 3D channel with length  $L$ , width  $w$ , and thickness  $t$

$$N(p) = 2 \times \frac{\frac{4}{3}\pi p^3}{\frac{h}{L} \frac{h}{w} \frac{h}{t}}, \quad (\text{B4})$$

which in conjunction with Eq. (B2) gives

$$D v = 2 \times \frac{2\pi p}{h^2} w, \quad (\text{for a 2D channel}), \quad (\text{B5a})$$

$$D v = 2 \times \frac{4\pi p^2}{h^3} wt, \quad (\text{for a 3D channel}), \quad (\text{B5b})$$

where  $D = D_0/L$  represents the density of states per unit length. Here, the prefactor 2 is introduced for two types of spins.

Combining Eqs. (B5a)–(B5b) with Eq. (3), which in conjunction with Eq. (B2), gives

$$M_T = 2 \times \frac{p}{\pi \hbar} w, \quad (\text{for a 2D channel}), \quad (\text{B6a})$$

$$M_T = 2 \times \frac{p^2}{4\pi \hbar^2} wt, \quad (\text{for a 3D channel}). \quad (\text{B6b})$$

At the Fermi energy, we can write  $p = \hbar k_F$  in terms of the Fermi wavevector  $k_F$ .  $k_F$  is related to the carrier concentration in the channel as [28]

$$k_F = \sqrt{2\pi n_s}, \quad (\text{for a 2D channel}), \quad (\text{B7a})$$

$$k_F = \sqrt[3]{3\pi^2 n}, \quad (\text{for a 3D channel}), \quad (\text{B7b})$$

where  $n_s$  and  $n$  are the carrier concentrations for a 2D and a 3D channel. Combining Eqs. (B7a)–(B7b) to Eqs. (B6a)–(B6b) yields the expressions in Eq. (4).

### APPENDIX C: SPIN-MOMENTUM LOCKING IN RASHBA CHANNELS

We start from the following Rashba Hamiltonian

$$\mathcal{H} = \frac{\hbar^2 k^2}{2m^*} I_{2 \times 2} - \alpha_R (\vec{\sigma} \times \vec{k}) \cdot \hat{y}, \quad (\text{C1})$$

where  $\alpha_R$  is the Rashba coefficient,  $m^*$  is the effective electron mass,  $k$  is the wave vector, and  $I_{2 \times 2}$  is a  $2 \times 2$  identity



matrix. The dispersion relation from Eq. (C1) is given by

$$E = \frac{\hbar^2 k^2}{2m^*} - s \alpha_R k, \quad (\text{C2})$$

with  $s$  being the spin index.

Solutions for  $k$  for a given energy  $E$  are given by

$$\begin{aligned} \hbar^2 k_1 &= s m^* \alpha_R + \sqrt{(m^*)^2 \alpha_R^2 + 2 \hbar^2 m^* E}, \\ \hbar^2 k_2 &= s m^* \alpha_R - \sqrt{(m^*)^2 \alpha_R^2 + 2 \hbar^2 m^* E}, \end{aligned}$$

noting that  $s^2 = 1$ .

Here,  $k_1(s = +1)$  and  $k_1(s = -1)$  correspond to  $M$  and  $N$  respectively. Similarly  $k_2(s = -1)$  and  $k_2(s = +1)$  correspond to  $M$  and  $N$ , respectively, satisfying the time-reversal symmetry. Thus the degree of SML  $p_0$  is given by

$$\begin{aligned} p_0(E_F) &= \frac{k_1(s = +1) - k_1(s = -1)}{k_1(s = +1) + k_1(s = -1)} \\ &= \frac{\alpha_R}{\sqrt{\alpha_R^2 + \frac{2 \hbar^2 E_F}{m^*}}}, \end{aligned} \quad (\text{C3})$$

which in conjunction with  $E_F = (1/2)m^*v_F^2$  gives the expression in Eq. (6).

- 
- [1] C. H. Li, O. M. van 't Erve, J. T. Robinson, Y. Liu, L. Li, and B. T. Jonker, Electrical detection of charge-current-induced spin polarization due to spin-momentum locking in  $\text{Bi}_2\text{Se}_3$ , *Nat. Nanotechnol.* **9**, 20325 (2014).
- [2] J. Tang, L.-T. Chang, X. Kou, K. Murata, E. S. Choi, M. Lang, Y. Fan, Y. Jiang, M. Montazeri, W. Jiang, Y. Wang, L. He, and K. L. Wang, Electrical detection of spin-polarized surface states conduction in  $(\text{Bi}_{0.53}\text{Sb}_{0.47})_2\text{Te}_3$  topological insulator, *Nano Lett.* **14**, 5423 (2014).
- [3] A. Dankert, J. Geurs, M. V. Kamalakar, S. Charpentier, and S. P. Dash, Room temperature electrical detection of spin polarized currents in topological insulators, *Nano Lett.* **15**, 7976 (2015).
- [4] L. Liu, A. Richardella, I. Garate, Y. Zhu, N. Samarth, and C.-T. Chen, Spin-polarized tunneling study of spin-momentum locking in topological insulators, *Phys. Rev. B* **91**, 235437 (2015).
- [5] J. Tian, I. Miotkowski, S. Hong, and Y. P. Chen, Electrical injection and detection of spin-polarized currents in topological insulator  $\text{Bi}_2\text{Te}_2\text{Se}$ , *Sci. Rep.* **5**, 14293 (2015).
- [6] J. S. Lee, A. Richardella, D. R. Hickey, K. A. Mkhoyan, and N. Samarth, Mapping the chemical potential dependence of current-induced spin polarization in a topological insulator, *Phys. Rev. B* **92**, 155312 (2015).
- [7] F. Yang, S. Ghatak, A. A. Taskin, K. Segawa, Y. Ando, M. Shiraishi, Y. Kanai, K. Matsumoto, A. Rosch, and Y. Ando, Switching of charge-current-induced spin polarization in the topological insulator  $\text{BiSbTeSe}_2$ , *Phys. Rev. B* **94**, 075304 (2016).
- [8] J.-H. Lee, H.-J. Kim, J. Chang, S. H. Han, H.-C. Koo, S. Sayed, S. Hong, and S. Datta, Multi-terminal spin valve in a strong Rashba channel exhibiting three resistance states, *Sci. Rep.* **8**, 3397 (2018).
- [9] Y. H. Park, H. Cheol Jang, H. C. Koo, H.-j. Kim, J. Chang, S. H. Han, and H.-J. Choi, Observation of gate-controlled spin-orbit interaction using a ferromagnetic detector, *J. Appl. Phys.* **111**, 07C317 (2012).
- [10] V. Vlamincck, J. E. Pearson, S. D. Bader, and A. Hoffmann, Dependence of spin-pumping spin Hall effect measurements on layer thicknesses and stacking order, *Phys. Rev. B* **88**, 064414 (2013).
- [11] W. Zhang, W. Han, X. Jiang, S.-H. Yang, and S. S. P. Parkin, Role of transparency of platinum-ferromagnet interfaces in determining the intrinsic magnitude of the spin Hall effect, *Nat. Phys.* **11**, 496 (2015).
- [12] M.-H. Nguyen, C.-F. Pai, K. X. Nguyen, D. A. Muller, D. C. Ralph, and R. A. Buhrman, Enhancement of the anti-damping spin torque efficacy of platinum by interface modification, *Appl. Phys. Lett.* **106**, 222402 (2015).
- [13] L. Liu, C.-F. Pai, Y. Li, H. W. Tseng, D. C. Ralph, and R. A. Buhrman, Spin-torque switching with the giant spin Hall effect of tantalum, *Science* **336**, 555 (2012).
- [14] C.-F. Pai, L. Liu, Y. Li, H. W. Tseng, D. C. Ralph, and R. A. Buhrman, Spin transfer torque devices utilizing the giant spin Hall effect of tungsten, *Appl. Phys. Lett.* **101**, 122404 (2012).
- [15] Y. Liu, B. Zhou, and J.-G. Zhu, Field-free magnetization switching by utilizing the spin Hall effect and inter-layer exchange coupling of iridium, *Sci. Rep.* **9**, 325 (2019).
- [16] Y. Niimi, M. Morota, D. H. Wei, C. Deranlot, M. Basletic, A. Hamzic, A. Fert, and Y. Otani, Extrinsic Spin Hall Effect Induced by Iridium Impurities in Copper, *Phys. Rev. Lett.* **106**, 126601 (2011).
- [17] Y. Niimi, Y. Kawanishi, D. H. Wei, C. Deranlot, H. X. Yang, M. Chshiev, T. Valet, A. Fert, and Y. Otani, Giant Spin Hall Effect Induced by Skew Scattering from Bismuth Impurities inside Thin Film Cubic Alloys, *Phys. Rev. Lett.* **109**, 156602 (2012).
- [18] Y. Niimi, H. Suzuki, Y. Kawanishi, Y. Omori, T. Valet, A. Fert, and Y. Otani, Extrinsic spin Hall effects measured with lateral spin valve structures, *Phys. Rev. B* **89**, 054401 (2014).
- [19] P. Li, W. Wu, Y. Wen, C. Zhang, J. Zhang, S. Zhang, Z. Yu, S. A. Yang, A. Manchon, and X.-X. Zhang, Spin-momentum locking and spin-orbit torques in magnetic nano-heterojunctions composed of Weyl semimetal  $\text{WTe}_2$ , *Nat. Commun.* **9**, 3990 (2018).
- [20] E. Lesne, Y. Fu, S. Oyarzun, J. C. Rojas-Sánchez, D. C. Vaz, H. Naganuma, G. Sicoli, J.-P. Attané, M. Jamet, E. Jacquet, J.-M. George, A. Barthélémy, H. Jaffrés, A. Fert, M. Bibes, and L. Vila, Highly efficient and tunable spin-to-charge conversion through Rashba coupling at oxide interfaces, *Nat. Mater.* **15**, 1261 (2016).
- [21] H. Yang, B. Zhang, X. Zhang, X. Yan, W. Cai, Y. Zhao, J. Sun, K. L. Wang, D. Zhu, and W. Zhao, Giant

- Charge-To-Spin Conversion Efficiency in SrTiO<sub>3</sub>-Based Electron gas Interface, *Phys. Rev. Appl.* **12**, 034004 (2019).
- [22] A. S. Everhardt, M. DC, X. Huang, S. Sayed, T. A. Gosavi, Y. Tang, C.-C. Lin, S. Manipatruni, I. A. Young, S. Datta, J.-P. Wang, and R. Ramesh, Tunable charge to spin conversion in strontium iridate thin films, *Phys. Rev. Mater.* **3**, 051201 (2019).
- [23] T. Nan, T. J. Anderson, J. Gibbons, K. Hwang, N. Campbell, H. Zhou, Y. Q. Dong, G. Y. Kim, D. F. Shao, T. R. Paudel, N. Reynolds, X. J. Wang, N. X. Sun, E. Y. Tsymbal, S. Y. Choi, M. S. Rzchowski, Y. B. Kim, D. C. Ralph, and C. B. Eom, Anisotropic spin-orbit torque generation in epitaxial SrIrO<sub>3</sub> by symmetry design, *PNAS* **116**, 16186 (2019).
- [24] S. Fukami, C. Zhang, S. DuttaGupta, A. Kurenkov, and H. Ohno, Magnetization switching by spin-orbit torque in an antiferromagnet-ferromagnet bilayer system, *Nat. Mater.* **15**, 535 (2016).
- [25] K. Gotlieb, C.-Y. Lin, M. Serbyn, W. Zhang, C. L. Smallwood, C. Jozwiak, H. Eisaki, Z. Hussain, A. Vishwanath, and A. Lanzara, Revealing hidden spin-momentum locking in a high-temperature cuprate superconductor, *Science* **362**, 1271 (2018).
- [26] S. Manipatruni, D. E. Nikonov, C.-C. Lin, T. A. Gosavi, H. Liu, B. Prasad, Y.-L. Huang, E. Bonturim, R. Ramesh, and I. A. Young, Scalable energy-efficient magnetoelectric spin-orbit logic, *Nature* **565**, 35 (2019).
- [27] S. Sayed, S. Hong, E. E. Marinero, and S. Datta, Proposal of a single nano-magnet memory device, *IEEE Electron. Device Lett.* **38**, 1665 (2017).
- [28] S. Sayed, S. Hong, and S. Datta, Transmission-Line Model for Materials with Spin-Momentum Locking, *Phys. Rev. Appl.* **10**, 054044 (2018).
- [29] S. Datta, *Lessons from Nanoelectronics: A New Perspective on Transport* (World Scientific Publishing Co. Pte. Ltd., Singapore, 2012).
- [30] E. K. de Vries, A. M. Kamerbeek, N. Koirala, M. Brahlek, M. Salehi, S. Oh, B. J. van Wees, and T. Banerjee, Towards the understanding of the origin of charge-current-induced spin voltage signals in the topological insulator Bi<sub>2</sub>Se<sub>3</sub>, *Phys. Rev. B* **92**, 201102 (2015).
- [31] L. Liu, C.-T. Chen, and J. Z. Sun, Spin Hall effect tunnelling spectroscopy, *Nat. Phys.* **10**, 561 (2014).
- [32] V. T. Pham, L. Vila, G. Zahnd, A. Marty, W. Savero-Torres, M. Jamet, and J.-P. Attané, Ferromagnetic/nonmagnetic nanostructures for the electrical measurement of the spin Hall effect, *Nano Lett.* **16**, 6755 (2016).
- [33] M. Isasa, M. C. Martínez-Velarte, E. Villamor, C. Magén, L. Morellón, J. M. De Teresa, M. R. Ibarra, G. Vignale, E. V. Chulkov, E. E. Krasovskii, L. E. Hueso, and F. Casanova, Origin of inverse Rashba-Edelstein effect detected at the Cu/Bi interface using lateral spin valves, *Phys. Rev. B* **93**, 014420 (2016).
- [34] J. Kim, C. Jang, X. Wang, J. Paglione, S. Hong, J. Lee, H. Choi, and D. Kim, Electrical detection of the surface spin polarization of the candidate topological Kondo insulator SmB<sub>6</sub>, *Phys. Rev. B* **99**, 245148 (2019).
- [35] K. Y. Camsari, S. Ganguly, and S. Datta, Modular approach to spintronics, *Sci. Rep.* **5**, 10571 (2015).
- [36] Y.-T. Chen, S. Takahashi, H. Nakayama, M. Althammer, S. T. B. Goennenwein, E. Saitoh, and G. E. W. Bauer, Theory of spin hall magnetoresistance, *Phys. Rev. B* **87**, 144411 (2013).
- [37] A. R. Mellnik, J. S. Lee, A. Richardella, J. L. Grab, P. J. Mintun, M. H. Fischer, A. Vaezi, A. Manchon, E.-A. Kim, N. Samarth, and D. C. Ralph, Spin-transfer torque generated by a topological insulator, *Nature* **511**, 449 (2014).
- [38] O. Mosendz, J. E. Pearson, F. Y. Fradin, G. E. W. Bauer, S. D. Bader, and A. Hoffmann, Quantifying Spin Hall Angles from Spin Pumping: Experiments and Theory, *Phys. Rev. Lett.* **104**, 046601 (2010).
- [39] P. Deorani and H. Yang, Role of spin mixing conductance in spin pumping: Enhancement of spin pumping efficiency in Ta/Cu/Py structures, *Appl. Phys. Lett.* **103**, 232408 (2013).
- [40] S. Sayed, S. Hong, and S. Datta, Multi-terminal spin valve on channels with spin-momentum locking, *Sci. Rep.* **6**, 35658 (2016).
- [41] S. Hong, V. Diep, S. Datta, and Y. P. Chen, Modeling potentiometric measurements in topological insulators including parallel channels, *Phys. Rev. B* **86**, 085131 (2012).
- [42] V. T. Pham, G. Zahnd, A. Marty, W. Savero Torres, M. Jamet, P. Noël, L. Vila, and J. P. Attané, Electrical detection of magnetic domain walls by inverse and direct spin hall effect, *Appl. Phys. Lett.* **109**, 192401 (2016).
- [43] E. Villamor, M. Isasa, L. E. Hueso, and F. Casanova, Contribution of defects to the spin relaxation in copper nanowires, *Phys. Rev. B* **87**, 094417 (2013).
- [44] B.-C. Lin, S. Wang, A.-Q. Wang, Y. Li, R.-R. Li, K. Xia, D. Yu, and Z.-M. Liao, Electric Control of Fermi arc Spin Transport in Individual Topological Semimetal Nanowires, *Phys. Rev. Lett.* **124**, 116802 (2020).
- [45] Z. Ren, A. A. Taskin, S. Sasaki, K. Segawa, and Y. Ando, Large bulk resistivity and surface quantum oscillations in the topological insulator Bi<sub>2</sub>Te<sub>2</sub>Se, *Phys. Rev. B* **82**, 241306 (2010).
- [46] N. W. Ashcroft and N. D. Mermin, *Solid State Physics* (Saunders, Philadelphia, 1976).
- [47] G. Fischer, H. Hoffmann, and J. Vancea, Mean free path and density of conductance electrons in platinum determined by the size effect in extremely thin films, *Phys. Rev. B* **22**, 6065 (1980).
- [48] P. Gargiani, S. Lisi, M. G. Betti, A. T. Ibrahimi, F. Bertran, P. Le Fèvre, and L. Chiodo, Orbital dependent Rashba splitting and electron-phonon coupling of 2d Bi phase on Cu(100) surface, *J. Chem. Phys.* **139**, 184707 (2013).
- [49] D. R. Penn and M. D. Stiles, Spin transport for spin diffusion lengths comparable to mean free paths, *Phys. Rev. B* **72**, 212410 (2005).
- [50] D. Gall, Electron mean free path in elemental metals, *J. Appl. Phys.* **119**, 085101 (2016).
- [51] S. Datta, *Electronic Transport in Mesoscopic Systems* (Cambridge University Press, Cambridge, 1997).
- [52] M. Bahramy, P. King, A. de la Torre, J. Chang, M. Shi, L. Pathney, G. Balakrishnan, P. Hofmann, R. Arita, N. Nagaosa, and F. Baumberger, Emergent quantum confinement at topological insulator surfaces, *Nat. Commun.* **3**, 1159 (2012).

- [53] J. Tian, S. Hong, S. Sayed, J. S. Lee, S. Datta, N. Samarth, and Y. P. Chen, On the understanding of current-induced spin polarization of three-dimensional topological insulators, *Nat. Commun.* **10**, 1461 (2019).
- [54] B. Yan, B. Stadtmüller, N. Haag, S. Jakobs, J. Seidel, D. Jungkenn, S. Mathias, M. Cinchetti, M. Aeschlimann, and C. Felser, Topological states on the gold surface, *Nat. Commun.* **6**, 10167 (2015).
- [55] C. R. Ast, J. Henk, A. Ernst, L. Moreschini, M. C. Falub, D. Pacilé, P. Bruno, K. Kern, and M. Grioni, Giant Spin Splitting through Surface Alloying, *Phys. Rev. Lett.* **98**, 186807 (2007).
- [56] H. J. Zhang, S. Yamamoto, Y. Fukaya, M. Maekawa, H. Li, A. Kawasuso, T. Seki, E. Saitoh, and K. Takanashi, Current-induced spin polarization on metal surfaces probed by spin-polarized positron beam, *Sci. Rep.* **4**, 4844 (2014).
- [57] M. Hoesch, M. Muntwiler, V. N. Petrov, M. Hengsberger, L. Patthey, M. Shi, M. Falub, T. Greber, and J. Osterwalder, Spin structure of the Shockley surface state on Au(111), *Phys. Rev. B* **69**, 241401 (2004).
- [58] A. Tamai, W. Meevasana, P. D. C. King, C. W. Nicholson, A. de la Torre, E. Rozbicki, and F. Baumberger, Spin-orbit splitting of the Shockley surface state on Cu(111), *Phys. Rev. B* **87**, 075113 (2013).
- [59] E. Sagasta, Y. Omori, S. Vélez, R. Llopis, C. Tollan, A. Chuvilin, L. E. Hueso, M. Gradhand, Y. Otani, and F. Casanova, Unveiling the mechanisms of the spin Hall effect in Ta, *Phys. Rev. B* **98**, 060410 (2018).
- [60] J. Sinova, S. O. Valenzuela, J. Wunderlich, C. H. Back, and T. Jungwirth, Spin hall effects, *Rev. Mod. Phys.* **87**, 1213 (2015).
- [61] A. Hoffmann, Spin Hall effects in metals, *IEEE Trans. Magn.* **49**, 5172 (2013).
- [62] W.-B. Liao, T.-Y. Chen, Y. Ferrante, S. S. P. Parkin, and C.-F. Pai, Current-induced magnetization switching by the high spin Hall conductivity  $\alpha$ -W, *Phys. Status Solidi RRL* **13**, 1900408 (2019).
- [63] Y. S. Kim, M. Brahlek, N. Bansal, E. Edrey, G. A. Kapilevich, K. Iida, M. Tanimura, Y. Horibe, S.-W. Cheong, and S. Oh, Thickness-dependent bulk properties and weak antilocalization effect in topological insulator  $\text{Bi}_2\text{Se}_3$ , *Phys. Rev. B* **84**, 073109 (2011).
- [64] J. Suh, K. M. Yu, D. Fu, X. Liu, F. Yang, J. Fan, D. J. Smith, Y.-H. Zhang, J. K. Furdyna, C. Dames, W. Walukiewicz, and J. Wu, Simultaneous enhancement of electrical conductivity and thermopower of  $\text{Bi}_2\text{Te}_3$  by multifunctionality of native defects, *Adv. Mater.* **27**, 3681 (2015).
- [65] J. Liu, J.-H. Chu, C. R. Serrao, D. Yi, J. Koralek, C. Nelson, C. Frontera, D. Kriegner, L. Horak, E. Arenholz, J. Orenstein, A. Vishwanath, X. Marti, and R. Ramesh, Tuning the electronic properties of  $j_{\text{eff}} = 1/2$  correlated semimetal in epitaxial perovskite  $\text{SrIrO}_3$ , arXiv:1305.1732 [cond-mat.str-el] (2013).
- [66] D. Cui, Y. Xu, L. Zhou, L. Zhang, Z. Luan, C. Li, D. Wu, and D. Wu, Electrically tunable inverse spin hall effect in  $\text{SrIrO}_3/\text{Pb}(\text{Mg}_{1/3}\text{Nb}_{2/3})_{0.7}\text{Ti}_{0.3}\text{O}_3$  heterostructures through interface strain coupling, *Appl. Phys. Lett.* **118**, 052904 (2021).
- [67] S. N. Panda, S. Mondal, J. Sinha, S. Choudhury, and A. Barman, All-optical detection of interfacial spin transparency from spin pumping in  $\beta$ -Ta/CoFeB thin films, *Sci. Adv.* **5**, eaav7200 (2019).
- [68] H. L. Wang, C. H. Du, Y. Pu, R. Adur, P. C. Hammel, and F. Y. Yang, Scaling of Spin Hall Angle in 3d, 4d, and 5d Metals from  $\text{Y}_3\text{Fe}_5\text{O}_{12}$ /metal Spin Pumping, *Phys. Rev. Lett.* **112**, 197201 (2014).
- [69] S. Cho, S.-h. C. Baek, K.-D. Lee, Y. Jo, and B.-G. Park, Large spin hall magnetoresistance and its correlation to the spin-orbit torque in W/CoFeB/MgO structures, *Sci. Rep.* **5**, 14668 (2015).
- [70] M. Belmeguenai, D. Apalkov, M. Gabor, F. Zighem, G. Feng, and G. Tang, Magnetic anisotropy and damping constant in CoFeB/Ir and CoFeB/Ru systems, *IEEE Trans. Magn.* **54**, 1 (2018).
- [71] M. Jamali, J. S. Lee, J. S. Jeong, F. Mahfouzi, Y. Lv, Z. Zhao, B. K. Nikolić, K. A. Mkhoyan, N. Samarth, and J.-P. Wang, Giant spin pumping and inverse spin Hall effect in the presence of surface and bulk spin-orbit coupling of topological insulator  $\text{Bi}_2\text{Se}_3$ , *Nano Lett.* **15**, 7126 (2015).
- [72] M. DC, R. Grassi, J.-Y. Chen, M. Jamali, D. R. Hickey, D. Zhang, Z. Zhao, H. Li, P. Quarterman, Y. Lv, M. Li, A. Manchon, K. A. Mkhoyan, T. Low, and J.-P. Wang, Room-temperature high spin-orbit torque due to quantum confinement in sputtered  $\text{Bi}_x\text{Se}_{(1-x)}$  films, *Nat. Mater.* **17**, 800 (2018).
- [73] S. Shi, S. Liang, Z. Zhu, K. Cai, S. D. Pollard, Y. Wang, J. Wang, Q. Wang, P. He, J. Yu, G. Eda, G. Liang, and H. Yang, All-electric magnetization switching and Dzyaloshinskii-Moriya interaction in  $\text{WTe}_2$ /ferromagnet heterostructures, *Nat. Nanotechnol.* **14**, 945 (2019).
- [74] J. Ibañez Azpiroz, A. Bergara, E. Y. Sherman, and A. Eiguren, Spin-flip transitions and departure from the Rashba model in the Au(111) surface, *Phys. Rev. B* **88**, 125404 (2013).
- [75] H. Y. Hung, G. Y. Luo, Y. C. Chiu, P. Chang, W. C. Lee, J. G. Lin, S. F. Lee, M. Hong, and J. Kwo, Detection of inverse spin Hall effect in epitaxial ferromagnetic  $\text{Fe}_3\text{Si}$  films with normal metals Au and Pt, *J. Appl. Phys.* **113**, 17C507 (2013).
- [76] O. Mosendz, V. Vlaminck, J. E. Pearson, F. Y. Fradin, G. E. W. Bauer, S. D. Bader, and A. Hoffmann, Detection and quantification of inverse spin hall effect from spin pumping in permalloy/normal metal bilayers, *Phys. Rev. B* **82**, 214403 (2010).
- [77] G. E. W. Bauer, Y. Tserkovnyak, D. Huertas-Hernando, and A. Brataas, Universal angular magnetoresistance and spin torque in ferromagnetic/normal metal hybrids, *Phys. Rev. B* **67**, 094421 (2003).
- [78] J. C. R. Sánchez, L. Vila, G. Desfonds, S. Gambarelli, J. P. Attané, J. M. De Teresa, C. Magén, and A. Fert, Spin-to-charge conversion using Rashba coupling at the interface between non-magnetic materials, *Nat. Commun.* **4**, 2944 (2013).
- [79] L. Zhu, D. C. Ralph, and R. A. Buhrman, Effective Spin-Mixing Conductance of Heavy-Metal-Ferromagnet Interfaces, *Phys. Rev. Lett.* **123**, 057203 (2019).
- [80] Y. Tserkovnyak, A. Brataas, and G. E. W. Bauer, Enhanced Gilbert Damping in Thin Ferromagnetic Films, *Phys. Rev. Lett.* **88**, 117601 (2002).

- [81] Y. Tserkovnyak, A. Brataas, G. E. W. Bauer, and B. I. Halperin, Nonlocal magnetization dynamics in ferromagnetic heterostructures, *Rev. Mod. Phys.* **77**, 1375 (2005).
- [82] K. Uchida, S. Takahashi, K. Harii, J. Ieda, W. Koshibae, K. Ando, S. Maekawa, and E. Saitoh, Observation of the spin Seebeck effect, *Nature* **455**, 778 (2008).
- [83] H. Adachi, K. ichi Uchida, E. Saitoh, and S. Maekawa, Theory of the spin Seebeck effect, *Rep. Prog. Phys.* **76**, 036501 (2013).
- [84] H. Tsai, S. Karube, K. Kondou, N. Yamaguchi, F. Ishii, and Y. Otani, Clear variation of spin splitting by changing electron distribution at non-magnetic metal/Bi<sub>2</sub>O<sub>3</sub> interfaces, *Sci. Rep.* **8**, 5564 (2018).
- [85] S. Oyarzún, A. K. Nandy, F. Rortais, J.-C. Rojas-Sánchez, M.-T. Dau, P. Noël, P. Laczkowski, S. Pouget, H. Okuno, L. Vila, C. Vergnaud, C. Beigné, A. Marty, J.-P. Attané, S. Gambarelli, J.-M. George, H. Jaffrès, S. Blügel, and M. Jamet, Evidence for spin-to-charge conversion by Rashba coupling in metallic states at the Fe/Ge(111) interface, *Nat. Commun.* **7**, 13857 (2016).
- [86] C. Cheng, M. Collet, J.-C. Rojas Sánchez, V. Ivanovskaya, B. Dlubak, P. Seneor, A. Fert, H. Kim, G. H. Han, Y. H. Lee, H. Yang, and A. Anane, Spin to charge conversion in MoS<sub>2</sub> monolayer with spin pumping, arXiv:1510.03451 [cond-mat.mes-hall] (2016).
- [87] H. Wang, J. Kally, J. S. Lee, T. Liu, H. Chang, D. R. Hickey, K. A. Mkhoyan, M. Wu, A. Richardella, and N. Samarth, Surface-State-Dominated Spin-Charge Current Conversion in Topological-Insulator-Ferromagnetic-Insulator Heterostructures, *Phys. Rev. Lett.* **117**, 076601 (2016).
- [88] M. DC, J.-Y. Chen, T. Peterson, P. Sahu, B. Ma, N. Mousavi, R. Harjani, and J.-P. Wang, Observation of high spin-to-charge conversion by sputtered bismuth selenide thin films at room temperature, *Nano Lett.* **19**, 4836 (2019).
- [89] C.-H. Lin, T.-R. Chang, R.-Y. Liu, C.-M. Cheng, K.-D. Tsuei, H. T. Jeng, C.-Y. Mou, I. Matsuda, and S. J. Tang, Rashba effect within the space-charge layer of a semiconductor, *New J. Phys.* **16**, 045003 (2014).
- [90] S. Bhandari, K. Wang, K. Watanabe, T. Taniguchi, P. Kim, and R. M. Westervelt, Imaging electron motion in a few layer MoS<sub>2</sub> device, *J. Phys. Conf. Ser.* **864**, 012031 (2017).
- [91] K. Lee, W. S. Yun, and J. D. Lee, Giant Rashba-type splitting in molybdenum-driven bands of MoS<sub>2</sub>/Bi(111) heterostructure, *Phys. Rev. B* **91**, 125420 (2015).
- [92] P. Ye, R. Yuan, Y. Y. Xia, and X. Zhao, Spin and valley transport in the ferromagnetic MoS<sub>2</sub> junctions subjected by the gate voltage, *J. Phys. Conf. Ser.* **827**, 012011 (2017).
- [93] C. Morrison, P. Wiśniewski, S. D. Rhead, J. Foronda, D. R. Leadley, and M. Myronov, Observation of Rashba zero-field spin splitting in a strained germanium 2d hole gas, *Appl. Phys. Lett.* **105**, 182401 (2014).
- [94] P. Jacquod, R. S. Whitney, J. Meair, and M. Büttiker, Onsager relations in coupled electric, thermoelectric, and spin transport: The tenfold way, *Phys. Rev. B* **86**, 155118 (2012).
- [95] T. S. Safi, P. Zhang, Y. Fan, Z. Guo, J. Han, E. R. Rosenberg, C. Ross, Y. Tserkovnyak, and L. Liu, Variable spin-charge conversion across metal-insulator transition, *Nature Commun.* **11**, 476 (2020).
- [96] D. Ruzmetov, D. Heiman, B. B. Claflin, V. Narayanamurti, and S. Ramanathan, Hall carrier density and magnetoresistance measurements in thin-film vanadium dioxide across the metal-insulator transition, *Phys. Rev. B* **79**, 153107 (2009).
- [97] J. B. S. Mendes, A. Aparecido-Ferreira, J. Holanda, A. Azevedo, and S. M. Rezende, Efficient spin to charge current conversion in the 2d semiconductor mos<sub>2</sub> by spin pumping from yttrium iron garnet, *Appl. Phys. Lett.* **112**, 242407 (2018).
- [98] A. Ruiz-Calaforra, T. Brächer, V. Lauer, P. Pirro, B. Heinz, M. Geilen, A. V. Chumak, A. Conca, B. Leven, and B. Hillebrands, The role of the non-magnetic material in spin pumping and magnetization dynamics in NiFe and CoFeB multilayer systems, *J. Appl. Phys.* **117**, 163901 (2015).